bioRxiv preprint doi: https://doi.org/10.1101/2020.02.23.961722; this version posted February 24, 2020. The copyright holder for this preprint (which was not certified by peer review) is the author/funder, who has granted bioRxiv a license to display the preprint in perpetuity. It is made available under aCC-BY-NC-ND 4.0 International license.

Control of endoplasmic reticulum membrane biogenesis by regulators of lipid metabolism

Peter W. Bircham[1,2,*], Dimitrios Papagiannidis[1,*], Christian Lüchtenborg[3], Giulia Ruffini[1], Britta Brügger[3], Sebastian Schuck[1]

[1] Center for Molecular Biology of Heidelberg University (ZMBH), DKFZ-ZMBH Alliance and CellNetworks Cluster of Excellence, 69120 Heidelberg, Germany

[2] present address: Laboratory of Systems Biology, VIB Center for Microbiology / Laboratory of Genetics and Genomics, CMPG, KU Leuven, 3001 Leuven, Belgium

[3] Biochemistry Center of Heidelberg University, 69120 Heidelberg, Germany

[*] these authors contributed equally

correspondence: Sebastian Schuck (ORCID 0000-0002-6388-0661), s.schuck@zmbh.uni-heidelberg.de, Center for Molecular Biology of Heidelberg University (ZMBH), Im Neuenheimer Feld 282, 69120 Heidelberg, Germany

keywords: organelle biogenesis, endoplasmic reticulum, URP, Opi1, lipin, yeast

bioRxiv preprint doi: https://doi.org/10.1101/2020.02.23.961722; this version posted February 24, 2020. The copyright holder for this preprint (which was not certified by peer review) is the author/funder, who has granted bioRxiv a license to display the preprint in perpetuity. It is made available under aCC-BY-NC-ND 4.0 International license.

ABSTRACT

Cells dynamically adapt organelle size to current physiological demand. Organelle growth and proliferation require membrane biogenesis and need to be coordinated with lipid metabolism. The endoplasmic reticulum (ER) can undergo massive expansion but the mechanisms that govern ER membrane biogenesis are unclear. Here, we genetically screen for factors mediating ER expansion in budding yeast and identify lipid synthesis enzymes and the ER transmembrane protein Ice2 as strong hits. Ice2 inhibits the conserved phosphatidic acid phosphatase Pah1 by opposing the activity of the Nem1-Spo7 complex. This regulation counteracts the production of storage lipids and directs lipid metabolism towards membrane biogenesis. Furthermore, Ice2 acts in concert with the transcriptional control of lipid synthesis enzymes and cooperates with the unfolded protein response to maintain ER homeostasis. These findings establish the regulation of the lipin ortholog Pah1 as a key determinant of ER membrane biogenesis.

bioRxiv preprint doi: https://doi.org/10.1101/2020.02.23.961722; this version posted February 24, 2020. The copyright holder for this preprint (which was not certified by peer review) is the author/funder, who has granted bioRxiv a license to display the preprint in perpetuity. It is made available under aCC-BY-NC-ND 4.0 International license.

INTRODUCTION

Cells reshape and resize their organelles when they undergo differentiation or adapt to changing conditions. An increase in organelle size or number typically involves enhanced membrane biogenesis, which in turn requires an adequate supply of membrane lipids. As a result, organelle biogenesis depends on whether cells employ available lipids as building blocks for new membranes, consume them for energy production or store them for future use. Accordingly, the mechanisms that control lipid synthesis and utilization are fundamental for organelle biogenesis and, consequently, for cell differentiation and adaptation.

The ER is a morphologically complex organelle with essential functions in protein folding and lipid synthesis (Westrate et al., 2015). It forms the nuclear envelope and extends into the cytoplasm as an interconnected network called the peripheral ER. The principal structural elements of the ER are tubules and sheets (Shibata et al., 2010). In addition, intermediate structures exist, such as tubular matrices and sheets with fenestrations or nanoholes (Puhka et al., 2012; Nixon-Abell et al., 2016; Schroeder et al., 2019). A variety of organelle morphologies can arise according to physiological demand, ranging from mainly tubular ER in lipid hormone-producing cells of the testis to mainly cisternal ER in secretory cells of the pancreas (Fawcett, 1981). ER size is also tuned to cellular need. The ER expands several-fold when B lymphocytes differentiate into antibody-secreting plasma cells or when cells face protein folding stress in the ER (Wiest et al., 1990; Bernales et al., 2006). Stress-induced ER expansion is mediated by signaling through the unfolded protein response (UPR), which induces genes encoding ER-resident protein folding enzymes to restore homeostasis (Walter and Ron, 2011). Besides determining the abundance of protein folding enzymes, the UPR also regulates the biogenesis of the ER membrane. It does so, at least in part, through the induction of genes that encode lipid synthesis enzymes (Sriburi et al., 2007; Bommiasamy et al., 2009; Schuck et al., 2009).

bioRxiv preprint doi: https://doi.org/10.1101/2020.02.23.961722; this version posted February 24, 2020. The copyright holder for this preprint (which was not certified by peer review) is the author/funder, who has granted bioRxiv a license to display the preprint in perpetuity. It is made available under aCC-BY-NC-ND 4.0 International license.

Yeast synthesize membrane phospholipids primarily from phosphatidic acid (PA) through the CDP-DAG pathway (Henry et al., 2012). Many enzymes of this pathway are controlled transcriptionally by the activators Ino2/4 and the repressor Opi1. Ino2 and Ino4 form a heterodimer that binds to promoter elements of lipid synthesis genes. Opi1 inhibits Ino2/4 by binding to Ino2 (Heyken et al., 2005). Repression of Ino2/4 by Opi1 is relieved when accumulating PA tethers Opi1 to the ER membrane and sequesters it away from the nucleoplasm (Loewen et al., 2004). The PA-Opi1-Ino2/4 system thus forms a feedback loop and matches PA availability to the cellular capacity for converting PA into other phospholipids. Removal of Opi1 results in activation of lipid synthesis and ER membrane expansion, even in cells lacking the UPR (Schuck et al., 2009). This membrane expansion without a corresponding upregulation of the protein folding machinery increases resistance to ER stress, highlighting the physiological importance of ER membrane biogenesis. However, it is unknown whether activation of Ino2/4 is the only mechanism relevant for ER membrane biogenesis. Furthermore, Ino2/4 and Opi1 are not conserved in metazoans. Lipid metabolism could therefore be regulated in unique ways in yeast. Alternatively, conserved lipid metabolism regulators unrelated to Ino2/4 and Opi1 could determine ER size in both yeast and higher eukaryotes.

Here, we systematically search for genes involved in ER membrane expansion in budding yeast, *Saccharomyces cerevisiae*, to better define the regulatory circuitry that connects lipid metabolism and organelle biogenesis.

bioRxiv preprint doi: https://doi.org/10.1101/2020.02.23.961722; this version posted February 24, 2020. The copyright holder for this preprint (which was not certified by peer review) is the author/funder, who has granted bioRxiv a license to display the preprint in perpetuity. It is made available under aCC-BY-NC-ND 4.0 International license.

RESULTS

An inducible system for ER membrane biogenesis

Removal of Opi1 induces Ino2/4-driven lipid synthesis genes and thereby leads to expansion of the ER (Schuck et al., 2009). To improve experimental control over ER membrane biogenesis, we developed an inducible system using ino2(L119A), which is an Ino2 variant that cannot be inhibited by Opi1 (Heyken et al., 2005). We placed ino2(L119A), here termed ino2*, under the control of the *GAL1* promoter and employed an expression system that activates this promoter upon addition of the metabolically inert sterol ß-estradiol (Pincus et al., 2014). High-level expression of ino2* is expected to displace endogenous Ino2 from the promoters of its target genes, stimulate lipid synthesis and drive ER membrane biogenesis (Figure 1A; Schuck et al., 2009). Fluorescence microscopy confirmed that expression of ino2* triggered pronounced ER expansion (Figure 1B). In untreated cells, the peripheral ER mostly consisted of tubules, which appeared as short membrane profiles along the cell cortex in optical mid sections and as a network in cortical sections. In contrast, estradiol-treated cells had a peripheral ER that predominantly consisted of ER sheets, as evident from long membrane profiles in mid sections and solid membrane areas in cortical sections.

To test whether ino2*-induced ER expansion causes ER stress, we measured UPR activity by means of a transcriptional reporter. This reporter is based on the UPR response element controlling expression of GFP (Jonikas et al., 2009). Treatment with the ER stressor DTT activated the UPR reporter, as expected, whereas expression of ino2* from the *GAL1* promoter did not (Figure 1C). Furthermore, expression of ino2* or removal of Opi1 did not alter the abundance of the chromosomally tagged ER proteins Sec63-mNeon or Rtn1-mCherry, even though Sec63 is encoded by a UPR-regulated gene (Figure 1D; Pincus et al., 2014). These observations indicate that ino2*-induced ER expansion is not an indirect consequence of ER stress but directly arises from enhanced lipid synthesis.

bioRxiv preprint doi: https://doi.org/10.1101/2020.02.23.961722; this version posted February 24, 2020. The copyright holder for this preprint (which was not certified by peer review) is the author/funder, who has granted bioRxiv a license to display the preprint in perpetuity. It is made available under aCC-BY-NC-ND 4.0 International license.

To assess ER membrane biogenesis quantitatively, we developed three metrics for the size of the peripheral ER at the cell cortex, as visualized in mid sections. These metrics are: (1) total area of the peripheral ER relative to cell periphery length, (2) mean length of individual ER profiles relative to cell periphery length and (3) number of gaps between ER profiles per micrometer cell periphery (Figure 1E). These new metrics are less sensitive to variation in image quality than the index of expansion we used previously (Schuck et al., 2009). Measurements of ER size upon induction of ino2* expression with different concentrations of estradiol showed a dose-dependent increase in total area and mean profile length, and a decrease in the number of gaps. At 800 nM estradiol, ER size was indistinguishable from that in *Δopi1* cells and we used this concentration in subsequent experiments. These results show that this inducible system allows titratable control of ER membrane biogenesis without causing ER stress.

A genetic screen for regulators of ER membrane biogenesis

To identify genes involved in ER expansion, we introduced the inducible ER biogenesis system and the ER markers Sec63-mNeon and Rtn1-mCherry into the knockout strain collection. This collection contains single deletion mutants for most of the approximately 4800 non-essential genes in yeast (Giaever et al., 2002). We induced ER expansion by ino2* expression and acquired images by high-throughput microscopy. Based on inspection of Sec63-mNeon images of optical mid sections, we defined six phenotypic classes. Mutants were grouped according to whether their ER was (1) underexpanded, (2) properly expanded and hence morphologically normal, (3) overexpanded, (4) overexpanded with extended cytosolic sheets, (5) overexpanded with disorganized cytosolic structures, or (6) clustered. Figure 2A shows two examples of each class. To refine the search for mutants with an underexpanded ER, we applied the three ER size metrics described above (Figure 2B and Table S1A). This computational analysis confirmed the underexpansion mutants identified visually and retrieved a number of additional, weaker hits. In total, we found 141 mutants that fell into at least one phenotypic class other than morphologically normal (Table S1B).

bioRxiv preprint doi: https://doi.org/10.1101/2020.02.23.961722; this version posted February 24, 2020. The copyright holder for this preprint (which was not certified by peer review) is the author/funder, who has granted bioRxiv a license to display the preprint in perpetuity. It is made available under aCC-BY-NC-ND 4.0 International license.

Hits included mutants lacking the ER-shaping gene *LNP1*, which had an overexpanded cortical ER with large gaps, and mutants lacking the *SEY1* gene important for homotypic ER fusion, which displayed ER clusters (Figure 2C; Hu et al., 2009; Chen et al., 2012). The re-identification of these known ER morphogenesis genes validated our screening approach. About two thirds of the identified mutants had an overexpanded ER, one third had an underexpanded ER and some showed ER clusters together with an otherwise underexpanded, normal or overexpanded ER (Figure 2D). Overexpansion mutants were significantly enriched in gene deletions that cause UPR activation (Table S1C; Jonikas et al., 2009). This enrichment suggested that ER expansion in these mutants results from ER stress and not enforced lipid synthesis. Indeed, re-imaging of the overexpansion mutants revealed that their ER was expanded also in the absence of ino2* (data not shown). Underexpansion mutants included those lacking *INO4*, as expected, or the known lipid synthesis genes *OPI3*, *CHO2* and *DGK1*. In addition, mutants lacking *ICE2* showed a particularly strong underexpansion phenotype (Figure 2B).

Overall, our screen showed that a large number of genes impinge on ER membrane biogenesis, as might be expected for a complex biological process. The functions of many of these genes in ER biogenesis remain to be uncovered. We here follow up on *ICE2* because of its apparent key role in building an expanded ER. In addition, Ice2 is a polytopic ER membrane protein and has previously been implicated in the formation or maintenance of the peripheral ER network (Estrada de Martin et al., 2005). Ice2 may thus have an immediate role in ER membrane biogenesis.

Ice2 promotes ER membrane biogenesis

To more precisely define the contribution of *ICE2* to ER membrane biogenesis, we analyzed optical sections of the cell cortex. Well-focused cortical sections are more difficult to acquire than mid sections but provide more morphological information. Qualitatively, deletion of *ICE2* had little effect on ER structure at steady state but severely impaired ER expansion upon ino2* expression (Figure 3A).

bioRxiv preprint doi: https://doi.org/10.1101/2020.02.23.961722; this version posted February 24, 2020. The copyright holder for this preprint (which was not certified by peer review) is the author/funder, who has granted bioRxiv a license to display the preprint in perpetuity. It is made available under aCC-BY-NC-ND 4.0 International license.

To describe ER morphology quantitatively, we developed a semi-automated algorithm that classifies ER structures as tubules or sheets based on images of Sec63-mNeon and Rtn1-mCherry in cortical sections (Figure 3B). First, the image of the general ER marker Sec63-mNeon is used to segment the total ER. Second, morphological opening, that is the operation of erosion followed by dilation, is applied to the segmented image to remove narrow structures. The structures removed by this step are defined as tubules and the remaining structures are provisionally classified as sheets. Third, the same procedure is applied to the image of Rtn1-mCherry, which marks high-curvature ER (Westrate et al., 2015). Rtn1 structures that remain after morphological opening and overlap with persistent Sec63 structures are termed tubular clusters. These structures appear as sheets in the Sec63 image but the overlap with Rtn1 identifies them as tubules. Tubular clusters made up only a minor fraction of the total ER and may correspond to so-called tubular matrices observed in mammalian cells (Nixon-Abell et al., 2016). Last, for a simple two-way classification, tubular clusters are added to the tubules and any remaining Sec63 structures are defined as sheets. This analysis using a general and a high-curvature ER marker allows densely packed tubules to be distinguished from sheets.

Application of this algorithm showed that the ER covered approximately 50% of the cell cortex in untreated wild-type cells and consisted mostly of tubules, in agreement with previous studies (Figure 3C; Schuck et al., 2009; West et al., 2011). Expression of ino2* triggered ER expansion by inducing the formation of sheets. *Δice2* cells had a defect in sheet formation already at steady state and membrane expansion upon ino2* expression failed almost completely. Importantly, activation of the prototypic Ino2/4 target gene *INO1* upon ino2* expression was intact in *Δice2* cells, ruling out that *ICE2* deletion disrupts the inducible ER biogenesis system (Figure 3D). In addition, *ICE2* deletion also abrogated the constitutive ER expansion in *Δopi1* cells, excluding that the expansion defect in *Δice2* cells merely reflects a delay (Figure 3E).

Next, we tested whether Ice2 is also required for ER expansion induced by ER stress. DTT treatment of wild-type cells triggered rapid ER expansion, which was

bioRxiv preprint doi: https://doi.org/10.1101/2020.02.23.961722; this version posted February 24, 2020. The copyright holder for this preprint (which was not certified by peer review) is the author/funder, who has granted bioRxiv a license to display the preprint in perpetuity. It is made available under aCC-BY-NC-ND 4.0 International license.

again driven by ER sheet formation (Figures 4A). Expansion appeared to be retarded in *Δice2* cells. Furthermore, induction of the UPR reporter by ER stress was reduced in *Δice2* cells, showing slowed UPR activation (Figure 4B). However, images of DTT-treated wild-type and *Δice2* cells revealed that ER expansion in *ice2* mutants was aberrant rather than delayed. Specifically, DTT induced the appearance of striking puncta positive for Rtn1-mCherry but not Sec63-mNeon, and these puncta were much more abundant in *Δice2* than in wild-type cells (Figure 4C-E). Hence, removal of Ice2 also impairs ER expansion during ER stress.

Finally, we asked whether raising Ice2 levels is sufficient to expand the ER. Indeed, *ICE2* overexpression caused ER expansion, and this still occurred in UPR-deficient *Δhac1* cells (Figure 4F; Emmerstorfer et al., 2015). In addition, *ICE2* overexpression did not activate the UPR (Figure 4G). These data show that Ice2 can drive ER membrane biogenesis independently of the UPR. However, the UPR could still function upstream of Ice2 and induce ER expansion by activating it.

Collectively, these data show that Ice2 is required for and promotes ER membrane biogenesis. These effects do not result from disrupted Ino2/4 target gene induction in the absence of Ice2 or from activation of the UPR upon *ICE2* overexpression.

Ice2 acts in the same pathway as Nem1, Spo7 and Pah1

Ice2 has been implicated in ER morphogenesis and lipid metabolism (Estrada de Martin et al., 2005; Tavassoli et al., 2013; Markgraf et al., 2014). In particular, Ice2 has been suggested to channel diacylglycerol (DAG) from lipid droplets (LDs) to the ER for membrane lipid synthesis (Markgraf et al., 2014). We therefore tested whether defective ER membrane biogenesis in *Δice2* cells could result from an insufficient supply of lipids from LDs. Deletion of *ICE2* causes a growth defect (Markgraf et al., 2014). Abolishing LD formation by combined deletion of *ARE1*, *ARE2*, *LRO1* and *DGA1* (Sandager et al., 2002) did not affect growth under our assay conditions, and deletion of *ICE2* still impaired growth in the absence of LDs (Figure S1A). Therefore, Ice2 must have functions that are independent of LDs.

bioRxiv preprint doi: https://doi.org/10.1101/2020.02.23.961722; this version posted February 24, 2020. The copyright holder for this preprint (which was not certified by peer review) is the author/funder, who has granted bioRxiv a license to display the preprint in perpetuity. It is made available under aCC-BY-NC-ND 4.0 International license.

Furthermore, lack of LDs had no effect on ER expansion after ino2* expression or DTT treatment, and deletion of *ICE2* still impaired ER expansion in the absence of LDs (Figure 5A, B). Hence, the role of Ice2 in ER membrane biogenesis cannot be explained by LD-related functions. These experiments additionally show that ER expansion can occur without lipid mobilization from LDs.

To define the functional context of Ice2, we carried out protein proximity screens using split-DHFR (Tarassov et al., 2008). An amino- or carboxy-terminal fragment of a methotrexate-resistant dihydrofolate reductase (DHFR*) was fused to the carboxy-terminus of Ice2. These Ice2 fusion proteins were functional as judged by growth assays (Figure S1B). The two Ice2-DHFR* variants were introduced into genome-wide strain collections in which the respective other DHFR* fragment was fused to every open reading frame. The resulting strains were grown in the presence of methotrexate, which blocks endogenous DHFR and prevents cell proliferation. Proximity of Ice2 and a protein fused to the other DHFR* fragment reconstitutes dihydrofolate reductase activity and restores growth (Figure 5C). To remove spurious hits, we performed identical screens with Hmg2, a polytopic ER membrane protein with similar abundance and distribution as Ice2 (Tkach et al., 2012). Proximity hits specific for Ice2 predominantly localized to the ER and included many proteins involved in lipid metabolism, including Cho1, Pis1, Spo7 and Ice2 itself (Figure 5C).

High-throughput studies have identified numerous genetic interactions between *ICE2* and lipid synthesis genes (Schuldiner et al., 2005; Costanzo et al., 2010; Surma et al., 2013). An interesting pattern emerged from mapping these genetic data onto the biochemical pathways for membrane biogenesis and lipid storage (Figure 5D and Table S2). *ICE2* displays negative interactions with genes for membrane lipid synthesis but positive interactions with *NEM1*, *SPO7* and *PAH1*, which together control the conversion of PA into DAG for lipid storage. Negative genetic interactions typically indicate involvement in parallel pathways relevant for the same biological process, whereas positive genetic interactions often reflect involvement in the same pathway (Costanzo et al., 2019).

bioRxiv preprint doi: https://doi.org/10.1101/2020.02.23.961722; this version posted February 24, 2020. The copyright holder for this preprint (which was not certified by peer review) is the author/funder, who has granted bioRxiv a license to display the preprint in perpetuity. It is made available under aCC-BY-NC-ND 4.0 International license.

In light of these data, we focused on *NEM1*, *SPO7* and *PAH1*. To validate the positive genetic interactions between these three genes and *ICE2*, we performed growth assays. Remarkably, the growth defect caused by *ICE2* deletion was completely suppressed by deletion of *NEM1*, *SPO7* or *PAH1*, confirming strong positive genetic interactions (Figures 5E and S2A, C). Next, we analyzed ER morphology. Deletion of *NEM1*, *SPO7* or *PAH1* drastically expands the ER and causes nuclear morphology defects (Siniossoglou et al., 1998; Santos-Rosa et al., 2005; Campbell et al., 2006). Additional deletion of *ICE2* in *Δnem1*, *Δspo7* or *Δpah1* cells had no effect on ER morphology, consistent with *ICE2* acting in the same pathway as the other three genes (Figures 5F and S2B, D). In contrast, deletion of *DGK1* rescued the aberrant ER morphology of *Δnem1*, *Δspo7* and *Δpah1* cells (Figure S2E). This was expected because Dgk1 opposes Nem1, Spo7 and Pah1 through a distinct pathway, namely the conversion of DAG into PA (Figure 5D; Han et al., 2008). In conclusion, *ICE2*, *NEM1*, *SPO7* and *PAH1* likely control ER membrane biogenesis as part of the same pathway.

Ice2 promotes ER membrane biogenesis by inhibiting Pah1

Pah1 is a phosphatidic acid phosphatase that converts PA into DAG (Figure 5D; Han et al. 2006). In yeast, PA is a precursor of all phospholipids, whereas DAG is the precursor of the storage lipid triacylglycerol (Henry et al., 2012). Pah1 thus promotes LD biogenesis (Figure 5D; Adeyo et al., 2011). Pah1 activity is regulated by reversible membrane association, which in turn depends on the phosphorylation status of Pah1 (Figure 6A). Phosphorylated Pah1 is cytosolic and inactive. Activation of Pah1 requires its dephosphorylation by the ER-localized phosphatase Nem1 in complex with Spo7. Pah1 can then associate with the ER membrane and gain access to its substrate, PA (O'Hara et al., 2006; Karanasios et al., 2010).

Even though Ice2 and Pah1 appear to act in the same pathway, deletion of *ICE2* impairs ER biogenesis whereas deletion of *PAH1* promotes it. These contrasting phenotypes raised the possibility that Ice2 inhibits Pah1. To test this idea, we separated different phospho-forms of Pah1 on Phos-tag gels and used the

bioRxiv preprint doi: https://doi.org/10.1101/2020.02.23.961722; this version posted February 24, 2020. The copyright holder for this preprint (which was not certified by peer review) is the author/funder, who has granted bioRxiv a license to display the preprint in perpetuity. It is made available under aCC-BY-NC-ND 4.0 International license.

phosphorylation status of Pah1 as a readout for its activity (Dubots et al., 2014). Removal of Ice2 strongly stimulated dephosphorylation of Pah1, and this effect was dependent on Nem1 (Figure 6B). These result suggests that Ice2 opposes the activity of the Nem1-Spo7 complex to restrain Pah1 activity.

We challenged this model in two ways. First, we compared the lipidome of wild-type, *Δice2*, *Δnem1* and *Δspo7* cells to determine whether they showed the expected shifts in the relative abundance of storage and membrane lipids. Compared with wild-type cells, *ice2* mutants had increased levels of ergosterol esters and triacylglycerol, the two lipid classes that make up LDs (Figure 6C, D). In contrast, the levels of the major phospholipids phosphatidylethanolamine and phosphatidylcholine were decreased. These changes agree with earlier data (Markgraf et al., 2014) and indicate that deletion of *ICE2*, and hence activation of Pah1, shifts lipid metabolism towards lipid storage. In contrast, *Δnem1* and *Δspo7* cells showed shifts in the opposite direction. These data confirm that removal of Nem1 or Spo7, and hence inactivation of Pah1, shifts lipid metabolism towards membrane biogenesis. The lipidomes of *Δnem1 Δice2* and *Δspo7 Δice2* double mutants were indistinguishable from those of *Δnem1* and *Δspo7* single mutants. These observations are consistent with the prediction that removal of Nem1 or Spo7 should abrogate the effects of their inhibitor Ice2.

As a second test of the above model, we asked whether the impact of Ice2 on ER biogenesis depends on inactivation of Pah1. We employed pah1(7A), which carries mutations in seven of the residues that are phosphorylated by various kinases and dephosphorylated by Nem1-Spo7 (O'Hara et al., 2006; Carman and Han, 2019). As a result, pah1(7A) displays constitutive activity, although some phospho-regulation by Nem1-Spo7 remains (Su et al., 2012). We quantified ER expansion upon *ICE2* overexpression in wild-type and pah1(7A)-expressing cells. Overexpression of *ICE2* in wild-type cells expanded the ER, as before (Figure 6E, also see Figure 4F). Replacement of Pah1 with pah1(7A) caused a slight shrinkage of the ER at steady state, consistent with reduced membrane biogenesis. Moreover, pah1(7A) almost completely blocked ER expansion upon *ICE2* overexpression. Similarly, pah1(7A) impaired ER expansion upon DTT treatment, almost completely phenocopying the

bioRxiv preprint doi: https://doi.org/10.1101/2020.02.23.961722; this version posted February 24, 2020. The copyright holder for this preprint (which was not certified by peer review) is the author/funder, who has granted bioRxiv a license to display the preprint in perpetuity. It is made available under aCC-BY-NC-ND 4.0 International license.

effects of *ICE2* deletion (Figures 6F, G and 4A, E). These data further support the idea that Ice2 contributes to ER membrane biogenesis by restricting Pah1 activity.

In summary, Ice2 inhibits Pah1 dephosphorylation by the Nem1-Spo7 complex, thereby promoting ER membrane biogenesis and opposing Pah1-mediated channeling of lipids towards LDs.

Ice2 cooperates with the PA-Opi1-Ino2/4 system and the UPR

Deletion of *OPI1* and overexpression of *ICE2* both cause ER expansion. These effects could be independent of each other or they could be linked. For instance, *ICE2* overexpression could inactivate Opi1 by causing an accumulation of PA (Loewen et al., 2004). However, combined deletion of *OPI1* and overexpression of *ICE2* produced an extreme ER expansion, which exceeded that in *Δopi1* mutants or *ICE2*-overexpressing cells (Figures 7A, B). This hyperexpanded ER covered most of the cell cortex and contained an even greater proportion of sheets than the ER in DTT-treated wild-type cells (Figures 7B and 4A). Therefore, the PA-Opi1-Ino2/4 system and Ice2 make independent contributions to ER membrane biogenesis.

Last, to gain insight into the physiological significance of Ice2, we analyzed the possible interplay between Ice2 and the UPR. UPR-deficient *Δhac1* mutants behaved like wild-type cells under standard growth conditions (Sidrauski et al., 1996) and *Δice2* cells showed a modest growth defect. However, *Δhac1 Δice2* cells grew worse than *Δice2* cells (Figure 7C). This synthetic phenotype indicates that Ice2 and the UPR cooperate to maintain ER homeostasis.

bioRxiv preprint doi: https://doi.org/10.1101/2020.02.23.961722; this version posted February 24, 2020. The copyright holder for this preprint (which was not certified by peer review) is the author/funder, who has granted bioRxiv a license to display the preprint in perpetuity. It is made available under aCC-BY-NC-ND 4.0 International license.

DISCUSSION

In this study, we identify factors involved in ER membrane expansion upon enforced lipid synthesis in yeast. Among these are the DAG kinase Dgk1, which generates PA for membrane biogenesis. Furthermore, we find that Ice2 is essential for proper ER expansion, both upon enforced lipid synthesis and during ER stress. We show that Ice2 inhibits the phosphatidic acid phosphatase Pah1 by opposing the activity of the Nem1-Spo7 phosphatase complex, thereby promoting membrane lipid synthesis. Finally, we provide evidence that Ice2 cooperates with the PA-Opi1-Ino2/4 system and the UPR to regulate ER membrane biogenesis and maintain ER homeostasis.

Together with earlier findings, our results help delineate a regulatory network controlling ER membrane biogenesis (Figure 7D). At the core of this network is the interconversion of DAG and PA by Dgk1 and Pah1. The activity of Pah1 depends on its dephosphorylation by the Nem1-Spo7 complex, which is opposed by Ice2. The Pah1-regulated production of the critical metabolic precursor PA is coordinated with the production of lipid synthesis enzymes that convert PA into other phospholipids. Active Pah1 directly represses Ino2/4-controlled lipid synthesis genes (Santos-Rosa et al., 2005). In addition, PA sequesters Opi1 and thereby derepresses Ino2/4 target genes (Loewen et al., 2004). Hence, Pah1 inactivation favors net PA production and both directly and indirectly induces lipid synthesis genes. Figuratively speaking, Pah1 is a shunt that diverts lipids to LDs, and Ice2 restricts the flow through this shunt to direct lipids towards ER membrane biogenesis.

The above model readily accounts for the available data on Ice2. The fact that *ICE2* deletion disrupts ino2*-driven ER expansion may be explained by the need to coordinate the production of lipid metabolic precursors with the expression of lipid synthesis genes. As we show, ino2* still induces genes encoding lipid synthesis enzymes in *ice2* mutants. Nevertheless, ER expansion fails, likely because the supply of substrates for these enzymes is insufficient. The same reasoning can explain the additive effects of *OPI1* deletion and *ICE2* overexpression on ER membrane biogenesis. *ICE2* overexpression favors PA production and presumably

bioRxiv preprint doi: https://doi.org/10.1101/2020.02.23.961722; this version posted February 24, 2020. The copyright holder for this preprint (which was not certified by peer review) is the author/funder, who has granted bioRxiv a license to display the preprint in perpetuity. It is made available under aCC-BY-NC-ND 4.0 International license.

382 releases some repression of Ino2/4 target genes. However, *OPI1* deletion likely
383 further boosts the abundance of lipid synthesis enzymes. Conversely, constitutive
384 Pah1 activation upon *ICE2* deletion can explain the increase in LD abundance in
385 *ice2* mutants (Markgraf et al., 2014), although our data do not exclude additional
386 roles of Ice2 in lipid mobilization from LDs. It now needs to be determined exactly
387 how Ice2 inhibits Pah1. A possibility consistent with our protein proximity data is that
388 Ice2 inhibits Spo7. However, we currently cannot exclude more indirect explanations,
389 for example that Ice2 activates a Pah1 kinase.
390
391 Changing physiological conditions impose an additional layer of control onto the
392 regulatory network outlined above. For instance, entry into stationary phase, when
393 cell division ceases, promotes LD formation at the expense of ER proliferation. In
394 contrast, growth resumption upon stationary phase exit is accompanied by LD
395 consumption and the biogenesis of new ER. These changes are brought about, at
396 least in part, through the phosphorylation of Pah1, Nem1 and possibly Dgk1 by
397 nutrient-responsive kinases (Kwiatek et al., 2020). Whether Ice2 activity is regulated
398 under these conditions needs to be explored. Another relevant setting is ER
399 membrane expansion during ER stress. Since ER expansion is unaffected in LD
400 mutants, it does not require lipid mobilization from LDs and can be fueled exclusively
401 by *de novo* lipid synthesis. This notion is supported by the upregulation of Ino2/4
402 target genes by ER stress (Schuck et al., 2009). In addition, *DGK1* is a UPR target
403 gene (Pincus et al., 2014) and the resulting increase in Dgk1 protein abundance
404 during ER stress presumably contributes to ER expansion. In contrast, the UPR
405 does not control the *ICE2* gene and it is a question for future investigation whether
406 and how ER stress regulates Ice2 and Pah1 activity. Interestingly, ER stress upon
407 inhibition of protein N-glycosylation can stimulate not only ER expansion but also LD
408 formation (Schuck et al., 2009; Fei et al., 2009; James et al., 2019). This may,
409 however, depend on exactly how N-glycosylation is perturbed (James et al., 2016).
410 The effects of ER stress on lipid droplet biogenesis clearly warrant further study.
411
412 Bioinformatic analysis using HHpred suggests mammalian SERINC proteins as
413 distant Ice2 orthologs (unpublished results). SERINC1 was initially proposed to be at

bioRxiv preprint doi: https://doi.org/10.1101/2020.02.23.961722; this version posted February 24, 2020. The copyright holder for this preprint (which was not certified by peer review) is the author/funder, who has granted bioRxiv a license to display the preprint in perpetuity. It is made available under aCC-BY-NC-ND 4.0 International license.

the ER, but later work detected SERINC proteins only at endosomes and the plasma membrane (Inuzuka et al., 2005; Rosa et al., 2015; Davies et al., 2018). Whether SERINC proteins have similar roles as Ice2 remains to be tested. In contrast, Nem1, Spo7 and Pah1 are known to be conserved (Han et al., 2012). The Pah1 orthologs lipin-1/2/3 are phospho-regulated in a similar manner as Pah1 and function in lipid storage in mice and humans (Harris and Fink, 2011; Zhang and Reue, 2017). Like in yeast, removal of lipins causes ER expansion in protozoa, plants, worms and flies (Golden et al., 2009; Eastmond et al., 2010; Bahmanyar et al., 2014; Grillet et al., 2016; Pillai et al., 2017). However, an important difference is that metazoans synthesize phospholipids mainly through the Kennedy pathway, which uses DAG and not PA as a precursor (McMaster, 2018). Therefore, DAG is a precursor for both LD and membrane biogenesis, seemingly ruling out the possibility that the balance between DAG and PA could determine whether LD or ER biogenesis is favored. This incongruence may be resolved by the finding from *A. thaliana* that CCT, the rate-limiting enzyme for phosphatidylcholine synthesis by the Kennedy pathway, is allosterically activated by PA (Craddock et al., 2015). Activation of CCT by PA may also exist in mice (Zhang et al., 2019). Thus, accumulation of PA may increase flux through the Kennedy pathway and channel DAG towards phospholipid synthesis (Jacquemyn et al., 2017). This model raises the unifying possibility that lipins inversely govern LD and ER biogenesis in all eukaryotes.

The regulation of lipid metabolism determines whether lipids are consumed, stored or used to build membranes. Elucidating how this decision is made will yield a deeper understanding of differentiation processes, for example the massive expansion of the ER during plasma cell development or the huge increase in LD abundance during adipogenesis. Moreover, it may enable therapeutic intervention in diseases associated with ER overload and aberrant lipid metabolism, such as diabetes and obesity. Besides organelle biogenesis, lipin activity has an impact on autophagy, axon regeneration, myopathy, dystonia and neurodegeneration (Zhang et al., 2014; Grillet et al., 2016; Zhang and Reue, 2017; Fanning et al., 2019; Yang et al., 2019; Schäfer et al., 2020). Unraveling the regulation of lipin will therefore have implications for a wide variety of cellular processes and associated diseases.

bioRxiv preprint doi: https://doi.org/10.1101/2020.02.23.961722; this version posted February 24, 2020. The copyright holder for this preprint (which was not certified by peer review) is the author/funder, who has granted bioRxiv a license to display the preprint in perpetuity. It is made available under aCC-BY-NC-ND 4.0 International license.

MATERIALS AND METHODS

Plasmids

Plasmids used in this study are listed in Table S3. To generate pNH605-P_{ADH1}-GEM-P_{GAL1}-ino2(L119A), the *ino2(L119A)* coding sequence was first subcloned from pRS415$_{MET25}$-ino2(L119A) into pRS416-P_{GAL1}. The P_{GAL1}-ino2(L119A)-T_{CYC1} cassette was then transferred into pNH605-P_{ADH1}-GEM. Similarly, pRS306-P_{ADH1}-GEM-P_{GAL1}-ino2(L119A) was generated by transferring the P_{GAL1}-ino2(L119A) cassette from pRS416-P_{GAL1}-ino2(L119A) into pRS306-P_{ADH1}-GEM. To generate pFA6a-mNeon-kanMX6 and pFA6a-mNeon-HIS3MX6, mNeonGreen (Shaner et al., 2013) was amplified from pFA6a-mNeon-kanMX4 and inserted into pFA6a-GFP(S65T)-kanMX6 and pFA6a-GFP(S65T)-HISMX6, replacing GFP(S65T). To generate pRS415-P_{ADH1}-Ice2, the *ICE2* coding sequence was amplified from yeast W303 genomic DNA and inserted into pRS415-P_{ADH1}. To generate expression plasmids for HA-tagged Pah1, YCplac111-Pah1-PrtA was linearized by inverse PCR and religated using the NEBuilder HiFi DNA assembly mix (New England Biolabs, Ipswitch, Massachusetts) such that the sequence encoding Protein A was replaced with a triple HA tag. A segment of the *pah1(7A)* coding sequence containing the seven alanine substitutions was amplified from YCPlac111-pah1(7A)-PrtA and inserted into YCPlac111-Pah1-3HA to yield YCplac111-pah1(7A)-3HA.

Yeast strain generation and growth

Strains used in this study are listed in Table S4. Strains generated for screening procedures were in the S288C background. All other strains were in the W303 background. Chromosomal modifications were introduced using PCR products or linearized plasmids (Longtine et al., 1998; Janke et al., 2004). The marker-free strains SSY2836 and SSY2837 were derived from SSY2809 by transformation with the *pah1(7A)-3HA* sequence amplified from plasmid pSS1047, followed by counterselection on 5-fluoroorotic acid.

Strains were grown at 30°C on YPD, SCD-MSG or SCD medium as indicated. YPD medium consisted of 1% yeast extract (Becton Dickinson, Heidelberg, Germany), 2% peptone (Becton Dickinson) and 2% glucose (Merck, Darmstadt, Germany). SCD-

bioRxiv preprint doi: https://doi.org/10.1101/2020.02.23.961722; this version posted February 24, 2020. The copyright holder for this preprint (which was not certified by peer review) is the author/funder, who has granted bioRxiv a license to display the preprint in perpetuity. It is made available under aCC-BY-NC-ND 4.0 International license.

MSG medium consisted of 0.17% yeast nitrogen base without amino acids and ammonium sulfate (Formedium, Norfolk, UK), 0.1% monosodium glutamate, amino acids and 2% glucose. SCD medium consisted of 0.7% yeast nitrogen base without amino acids (Sigma, Taufkirchen, Germany), amino acids and 2% glucose. Media contained antibiotics or lacked certain amino acids as appropriate for selection.

Light microscopy

Precultures were grown in liquid SCD medium during the day, diluted into fresh medium and grown overnight for 16 h so that they reached mid log phase (OD_{600} = 0.5 - 1). For induction of the GEM-GAL system, overnight cultures were diluted to OD_{600} = 0.05 in fresh medium and treated with the indicated concentrations of ß-estradiol (Sigma) for up to 6 h. For DTT treatment, overnight cultures were diluted to OD_{600} = 0.1 and treated with 8 mM DTT (Roche, Mannheim, Germany) for up to 2 h. Immediately before imaging, cells were harvested by centrifugation, mounted on coverslips and covered with a 1% (w/v) agarose pad. Images were acquired with a DMi8 inverted microscope (Leica, Wetzlar, Germany) equipped with a CSU-X1 spinning-disk confocal scanning unit (Yokogawa, Musashino, Japan) and an ORCA-Flash 4.0 LT camera (Hamamatsu, Hamamatsu, Japan). A HC PL APO 63x/1.40-0.60 or a HC PL APO 100x/1.4 CS2 oil objective lens (Leica) was used.

UPR assays

UPR activity was measured by flow cytometry as described in Schmidt et al., 2019. Cells expressing cytosolic BFP and the 4xUPRE-GFP transcriptional reporter for UPR activity (Jonikas et al., 2009) were grown to mid log phase. Where indicated, cells were treated with estradiol or DTT as above. Fluorescence was measured with a FACS Canto flow cytometer (BD Biosciences, Franklin Lakes, New Jersey) equipped with a high-throughput sampler. Background autofluorescence was determined with identically grown isogenic control strains not harboring the UPR reporter. Background-subtracted GFP fluorescence was divided by BFP fluorescence to account for differences in protein translation capacity. GFP/BFP ratios were normalized to untreated wild-type cells.

bioRxiv preprint doi: https://doi.org/10.1101/2020.02.23.961722; this version posted February 24, 2020. The copyright holder for this preprint (which was not certified by peer review) is the author/funder, who has granted bioRxiv a license to display the preprint in perpetuity. It is made available under aCC-BY-NC-ND 4.0 International license.

Cell lysis and western blotting

For standard western blotting, cells were harvested by centrifugation, washed once with water, resuspended in 50 mM HEPES pH 7.5 containing 0.5 mM EDTA, 1 mM PMSF and complete protease inhibitors (Roche), and disrupted with glass beads using a FastPrep 24 (MP Biomedicals). SDS was added to 1.5% (w/v) and proteins were solubilized by incubation at 65ºC for 5 min. Equal protein amounts, as determined with the BCA assay kit (Thermo Fisher Scientific Pierce, Waltham, Massachusetts), were resolved by SDS-PAGE and transferred onto nitrocellulose membranes. Membranes were probed with primary and HRP-coupled secondary antibodies and developed with homemade ECL. Chemiluminescence was detected with an ImageQuant LAS 4000 imaging system (GE Healthcare, Chalfont St Giles, UK). Primary antibodies were rabbit anti-Sec63 (Feldheim et al., 1992), mouse anti-mCherry 1C51 (Abcam, Cambridge, UK), mouse anti-Pgk1 22C5 (Abcam) and rat anti-HA 3F10 (Roche). To assess the phosphorylation status of Pah1, cells were lysed by alkaline extraction and incubation in a modified SDS-PAGE sample buffer at 65ºC for 3 min (Kushnirov, 2000). Proteins were resolved on Zn^{2+}-containing Phos-tag gels according to Nagy et al., 2018 with minor modifications. Gels contained 8% acrylamide/bisacrylamide (29:1), 25 μM Phos-tag acrylamide (Fujifilm Wako Chemicals, Neuss, Germany) and 50 μM $ZnCl_2$ in 350 mM Bis-Tris-HCl pH 6.8. Gels were run at 200 V at room temperature, washed 3 x 10 min in transfer buffer (25 mM Tris-HCl, 192 mM glycine, 20% methanol) containing 1 mM EDTA and 2 x 20 min in transfer buffer. Blotting was done at 100 V at 4ºC for 3 h.

Construction of diploid ER marker knockout library

Using strains SSY2589 and SSY2590, the ER marker proteins Sec63-mNeon and Rtn1-mCherry along with the GEM-P_{GAL1}-ino2* cassette were integrated into the yeast knockout collection through modified SGA methodology (Giaever et al., 2002; Tong and Boone 2007). SSY2589 and SSY2590 were independently mated to the knockout collection on YPD medium using a Singer RoToR robot. For each library, diploids were selected on SCD-MSG lacking uracil and containing G418. Cells were pinned onto enriched sporulation medium (1% potassium actetate, 0.1% yeast extract, 0.05% glucose, 0.01% amino acid supplement consisting of only histidine,

bioRxiv preprint doi: https://doi.org/10.1101/2020.02.23.961722; this version posted February 24, 2020. The copyright holder for this preprint (which was not certified by peer review) is the author/funder, who has granted bioRxiv a license to display the preprint in perpetuity. It is made available under aCC-BY-NC-ND 4.0 International license.

leucine, lysine and uracil) and kept at 23°C for 5 days. Haploids were selected by two rounds of pinning onto SCD-MSG lacking histidine/arginine/lysine with canavanine and thialysine or SCD-MSG lacking leucine/arginine/lysine with canavanine and thialysine to select for MATa (Sec63-mNeon library) and MATα (Rtn1-mCherry library) cells, respectively. Haploid cells harboring the required markers were selected by sequential pinning onto appropriate media. The two libraries were then mated together and diploids were selected on YPD containing nourseothricin and hygromycin to generate the final library with the genotype: *xxxΔ::kan/xxxΔ::kan SEC63-mNeon::HIS3/SEC63 RTN1-mCherry::nat/RTN1 can1Δ::GEM-*P_{GAL1}*-ino2*-URA3/can1Δ::*P_{STE2}*-HIS3 lyp1Δ::GEM-*P_{GAL1}*-ino2*-URA3/lyp1Δ::*P_{STE3}*-LEU2 his3Δ::*P_{GPD}*-TagBFP-hph/his3Δ0.* This diploid library afforded two benefits compared with a haploid library. The larger size of diploid cells facilitated acquisition of informative images and the fact that cells were heterozygous for the fluorescently tagged ER marker proteins reduced the risk that specious morphological phenotypes arose from impaired functionality of Sec63 or Rtn1.

High-throughput microscopy

Cells were grown to saturation overnight in 100 µl cultures in SCD medium in regular 96 well microtiter plates. Prior to imaging, 7 µl of culture was transferred into 1 ml fresh SCD medium containing 800 nM estradiol and grown for 5 h in 96 deep-well microtiter plates to reach logarithmic growth phase. One-hundred µl of each sample was transferred into 96 well glass bottomed microtiter plates (Brooks Life Sciences, Chelmsford, Massachusetts) coated with concanavalin A and allowed to attach. Medium was refreshed after 1 h to remove non-attached cells. Samples were imaged with a Nikon Ti-E wide-field microscope equipped with a motorized stage, a Nikon perfect focus system, a Flash4 Hamamatsu sCMOS camera and a 60x/1.49 oil immersion lens. For each sample, two fields of view were acquired consisting of five optical slices spaced 1 µm apart. Untreated wild-type control strains were included in duplicate on each plate as a reference for unexpanded ER.

Automated cell segmentation and peripheral ER size measurement

Image analysis was conducted in MATLAB using custom scripts. Initial cell objects

bioRxiv preprint doi: https://doi.org/10.1101/2020.02.23.961722; this version posted February 24, 2020. The copyright holder for this preprint (which was not certified by peer review) is the author/funder, who has granted bioRxiv a license to display the preprint in perpetuity. It is made available under aCC-BY-NC-ND 4.0 International license.

were identified based on the cytoplasmic BFP. The best overall mid-section image was selected by assessing the standard deviation in the BFP image, which is highest when the image is in focus. Next, a fast Fourier transformation and bandpass filter were used to enhance contrast at the cell border. A Frangi filter (based on the implementation by D.J. Kroon, “Hessian based Frangi Vesselness filter”, MATLAB Central File Exchange. Retrieved May 2017) followed by Otsu thresholding was then used to generate a mask of apparent cell borders. Morphological opening followed by a minimum size filter was used to remove false labeling created by yeast vacuoles. The resulting image highlighted the cell borders. Because the borders of many cells touched each other, the internal space was used to identify and separate the individual cell objects. The intensity of these initial cell objects was measured and only objects brighter than two median absolute deviations below the median were kept. Finally, any remaining touching cells, including connected mother cells and buds, were separated by watershedding. The segmentation of individual cell objects obtained through this procedure was then optimized to generate more accurate cell boundaries and peripheral ER segmentation. For this, cells were cropped and the best mid-section was reassessed on a per cell basis using the standard deviation of the Rtn1-mCherry image. The BFP images were re-segmented using the above procedure based on the new mid-section. To accurately define the cell periphery for image quantification, object borders were expanded but contained within watershed boundaries. The ER was segmented in both the Sec63-mNeon and Rtn1-mCherry images using a Frangi tubeness filter. A more accurate cell border was defined by fitting a minimum volume ellipse (based on the implementation by N. Moshtagh, “Minimum Volume Enclosing Ellipsoid”, MATLAB Central File Exchange. Retrieved July 2017) to the combined masks of the segmented ER. Based on this segmentation, cell area, mean Sec63-mNeon and Rtn1-mCherry fluorescence, and cell roundness were calculated. An area five pixels from the border was used to define the peripheral ER. From this, total ER area (peripheral ER area divided by cell periphery length), ER profile length (mean length of ER profiles divided by cell periphery length) and ER gaps (number of gaps in the peripheral ER mask per micrometer) were calculated. Finally, to remove false cell objects, poorly segmented cells and dead cells, all of these measurements were used to limit the cell population

bioRxiv preprint doi: https://doi.org/10.1101/2020.02.23.961722; this version posted February 24, 2020. The copyright holder for this preprint (which was not certified by peer review) is the author/funder, who has granted bioRxiv a license to display the preprint in perpetuity. It is made available under aCC-BY-NC-ND 4.0 International license.

to values within 2.5 standard deviations of the population mean. On average, 248 cells were analyzed per mutant, with the minimum being 25.

Visual ER morphology analysis

To identify mutants with aberrant ER morphology, images were assessed visually using a custom image viewer application made in MATLAB. Segmented cells were arrayed in a montage displaying 7 x 15 cells at a time. Any strains with abnormal ER morphology were re-imaged as described above to ensure that the phenotype was robust. ER morphologies were independently annotated by two individuals with one or more of the following features: underexpanded, overexpanded, extended sheets, disorganized and clustered.

Computational ER expansion analysis

Since most gene deletions did not affect ER expansion, mutants from the same imaging plate can serve as a plate-specific background population for comparison to individual deletion strains. Sec63-mNeon intensity was used to define this background population and exclude the influence of extreme outliers. First, to remove plate effects, mNeon intensities were normalized by subtracting the plate means. Next, values were corrected for cell size (bigger cells being brighter) and cell count (densely crowded areas having an overall higher fluorescence) by local regression. Finally, the background population (BP) was defined for each plate as mutants that were within 1.5 standard deviations of the mean. To normalize the ER expansion measurements, a Z score was calculated as (sample - BP mean)/BP standard deviation, thereby removing plate effects. The time spent imaging each plate (approximately 50 minutes) was accounted for by correcting for well order by local regression. Similarly, cell density effects were corrected for by local regression against cell count. Scores were calculated separately for each field of view and the maximum value was taken for each sample. False positives were removed by visual inspection, which were often caused by an out of focus field of view. Strains passing arbitrary thresholds of significance (Z score less than -2 for total ER area and ER profile length, and greater than 2 for ER gaps) in at least two of the measurements and no overall morphology defects as defined above were re-imaged in triplicate

bioRxiv preprint doi: https://doi.org/10.1101/2020.02.23.961722; this version posted February 24, 2020. The copyright holder for this preprint (which was not certified by peer review) is the author/funder, who has granted bioRxiv a license to display the preprint in perpetuity. It is made available under aCC-BY-NC-ND 4.0 International license.

638 along with wild-type control strains under both untreated and estradiol-treated
639 conditions. Images were inspected visually as a last filter to define the final list of
640 strains with ER expansion defects.
641
642 **Semi-automated cortical ER morphology quantification**
643 For cell segmentation, bright field images were processed in Fiji to enhance the
644 contrast of the cell periphery. For this, a Gaussian blur (sigma = 2) was applied to
645 reduce image noise, followed by a scaling down of the image (x = y = 0.5) to reduce
646 the effect of small details on cell segmentation. A tubeness filter (sigma = 1) was
647 used to highlight cell borders and the images were scaled back up to the original
648 resolution. Cells were segmented using CellX (Dimopoulos et al., 2014) and out of
649 focus cells were removed manually. A user interface in MATLAB was then used to
650 assist ER segmentation. Users input images of Sec63-mNeon and Rtn1-mCherry
651 from cortical sections (background subtracted in Fiji using the rolling ball method with
652 a radius of 50 pixels) and the cell segmentation file generated in CellX. Adjustable
653 parameters controlled the segmentation of ER tubules and sheets for each image.
654 These parameters were tubule radius, tubule strength and sheet background.
655 Manual fine-tuning of these parameters was important to ensure consistent ER
656 segmentation across images with different signal intensities. These parameters were
657 set independently for Sec63-mNeon and Rtn1-mCherry images together with one
658 additional parameter called ‘trimming factor’, which controls the detection of ER
659 sheets. ER masks were calculated across entire images and were assigned to
660 individual cells based on the CellX segmentation. For each channel, the background
661 (BG) levels were automatically calculated using Otsu thresholding and fine tuned by
662 multiplying the threshold value by the ‘tubule BG’ (Rtn1 channel) or ‘sheet BG’
663 (Sec63 channel) adjustment parameters. A 3x3 median filter was applied to
664 smoothen the images and reduce noise that is problematic for segmentation. Two
665 rounds of segmentation were passed for each image channel (Sec63 or Rtn1) with
666 one optimised for finding smaller features (i.e. ER tubules) and the other for larger
667 features (i.e. ER sheets). Firstly, convolution kernels were calculated for small and
668 large features, respectively, defined as a ring of radius +1, where the radius is given
669 in the ‘tubule radius’ (small feature) or ‘sheet radius’ (large feature) parameters.

bioRxiv preprint doi: https://doi.org/10.1101/2020.02.23.961722; this version posted February 24, 2020. The copyright holder for this preprint (which was not certified by peer review) is the author/funder, who has granted bioRxiv a license to display the preprint in perpetuity. It is made available under aCC-BY-NC-ND 4.0 International license.

These convolution kernels were applied pixel-wise to determine if a pixel is brighter than the mean intensity of the surrounding ring of pixels. The strength of this filter was fine-tuned by adjusting the 'tubule strength' or 'sheet strength' parameters. Additionally, segmented pixels had to be brighter than the background levels defined above. This procedure generated two segmented images per channel, which were then combined to generate the 'total ER' mask for that channel. To define which regions in each channel represented sheets or tubules a morphological opening was applied, the degree of which was controlled by the parameter 'trimming factor'. Features that remained in the Sec63 segmentation mask after morpholical opening were provisionally designated as sheets, whereas the remainder of the ER mask was designated tubules. Finally, areas that were sheet-like in the Rtn1 segmentation mask and overlapped with the Sec63 mask were designated tubular clusters. Tubular clusters were subtracted from provisonal sheets to obtain the final designation of sheets. The median size measurements of each class were taken from the whole cell population for further analyses.

Quantitative real-time PCR

Quantitative real-time PCR was done exactly as described (Schmidt et al., 2019).

Ice2 protein proximity screen

Ice2 proximity was screened by split DHFR protein complementation assay (Tarassov et al., 2008). Hmg2 served as a control for non-specific hits. *MATa ICE2-DHFR[1,2]* and *MATα ICE2-DHFR[3]* strains as well as the control strains *MATa HMG2-DHFR[1,2]* and *MATα HMG2-DHFR[3]* were mated to the library of the opposite mating type in 1536 colony format. Diploid cells were pinned onto SCD medium containing 200 μg/ml methotrexate (Merck). Colonies were grown for 4 days at 30°C before imaging using a Singer PhenoBooth with bottom illumination. Since methotrexate is light sensitive, plate preparation and cell growth were carried out in the dark. Data analysis was conducted in R. Colony size was measured using the Gitter package (Wagih and Parts, 2014). Raw colony size measurements were median polished to remove row and column effects. Z scores were calculated to remove plate effects. Scores were converted into p-values and subjected to

bioRxiv preprint doi: https://doi.org/10.1101/2020.02.23.961722; this version posted February 24, 2020. The copyright holder for this preprint (which was not certified by peer review) is the author/funder, who has granted bioRxiv a license to display the preprint in perpetuity. It is made available under aCC-BY-NC-ND 4.0 International license.

Benjamini Hochberg multiple testing correction with corrected p-values below 0.05 being considered significant. The Ice2 screen was conducted twice and the Hmg2 screen once. Proteins were considered hits if they were significant in three out of four possible outcomes (MATa and MATα libraries in duplicate). Proteins that were only present in one of the MAT type libraries were also considered hits if they were significant in both repeats. Finally, any proteins that were also hits in either of the Hmg2 libraries (MATa or MATα) were excluded.

Growth assays

For growth assays in liquid culture, cells were grown to saturation and diluted to OD_{600} = 0.05. For each strain, 500 μl culture was transferred into 48-well plates in triplicate and absorbance at 600 nm was measured at room temperature in 5 minute intervals for 24 hours using a Tecan Infinite M1000 Pro plate reader. The area under the curve was calculated with the R package Growthcurver (Sprouffske and Wagner, 2016) and used as a measure for cell growth. For the growth assays shown in Figure 7C, cells were grown to mid log phase, diluted as above and absorbance was measured at 30°C using a Tecan Spark Cyto plate reader. This experimental regime ensured that *Δhac1* mutants grew as well as wild-type cells.

Lipidomics

For each sample, approximately 2 x 10^8 cells (10 ODs) were harvested from cultures grown to mid log phase and snap frozen in liquid nitrogen. Cells were disrupted with glass beads as above in 50 mM HEPES pH 7.5 containing 0.5 mM EDTA. Aliquots were subjected to acidic Bligh and Dyer lipid extractions in the presence of internal lipid standards added from a master mix containing 40 pmol d7-PC mix (15:0/18:1-d7, Avanti Polar Lipids), 25 pmol PI (17:0/20:4, Avanti Polar Lipids), 25 pmol PE and 15 pmol PS (14:1/14:1, 20:1/20:1, 22:1/22:1, semi-synthesized as described in Özbalci et al., 2013), 20 pmol DAG (17:0/17:0, Larodan), 20 pmol TAG (D5-TAG-Mix, LM-6000 / D5-TAG 17:0,17:1,17:1, Avanti Polar Lipids), 20 pmol PA (PA 17:0/20:4, Avanti Polar Lipids), 5 pmol PG (14:1/14:1, 20:1/20:1, 22:1/22:1, semi-synthesized as described in Özbalci et al., 2013), 40 pmol ergosteryl ester (15:0 and 19:0, semi-synthesized as described in Gruber et al., 2018) and 20 pmol t-Cer (18:0,

bioRxiv preprint doi: https://doi.org/10.1101/2020.02.23.961722; this version posted February 24, 2020. The copyright holder for this preprint (which was not certified by peer review) is the author/funder, who has granted bioRxiv a license to display the preprint in perpetuity. It is made available under aCC-BY-NC-ND 4.0 International license.

734 Avanti Polar Lipids). Lipids recovered in the organic extraction phase were
735 evaporated by a gentle stream of nitrogen. Prior to measurements, lipid extracts
736 were dissolved in 10 mM ammonium acetate in methanol and transferred into
737 Eppendorf twin.tec 96-well plates. Mass spectrometric measurements were
738 performed in positive ion mode on an AB SCIEX QTRAP 6500+ mass spectrometer
739 equipped with chip-based (HD-D ESI Chip, Advion Biosciences) nano-
740 electrospray infusion and ionization (Triversa Nanomate, Advion Biosciences) as
741 described (Özbalci et al., 2013). The following precursor ion scanning (PREC) and
742 neutral loss scanning (NL) modes were used for the measurement of the various
743 lipid classes: +PREC 184 (PC), +PREC282 (t-Cer), +NL141 (PE), +NL185 (PS),
744 +NL277 (PI), + NL189 (PG), +NL115 (PA), +PREC 77 (ergosterol), +PREC379
745 (ergosteryl ester). Ergosterol was quantified following derivatization to ergosterol
746 acetate in the presence of 200 pmol of the internal standard (22E)-Stigmasta-5,7,22-
747 trien-3-beta-ol (Aldrich, R202967) using 100 μl acetic anhydride/chloroform (1:12 v/v)
748 overnight under argon atmosphere (Ejsing et al., 2009). Mass spectrometry settings:
749 Resolution: unit, low mass configuration; data accumulation: 400 MCA; curtain gas:
750 20; Interface heater temperature: 60; CAD: medium; DR: open; separation voltage:
751 3800; DMO: -3; compensation voltage: 10; DMS temperature: 60°C. Data evaluation
752 was done using LipidView (Sciex) and a software developed in house, ShinyLipids.

bioRxiv preprint doi: https://doi.org/10.1101/2020.02.23.961722; this version posted February 24, 2020. The copyright holder for this preprint (which was not certified by peer review) is the author/funder, who has granted bioRxiv a license to display the preprint in perpetuity. It is made available under aCC-BY-NC-ND 4.0 International license.

ACKNOWLEDGEMENTS

We thank Randy Schekman, Maya Schuldiner and Symeon Siniossoglou for reagents, Michael Knop for access to screening equipment, the ZMBH imaging facility for assistance, Oliver Pajonk, Dorottya Polos and Julia Schessner for contributions to early stages of this project, Iris Leibrecht for help with lipidomics analyses, and Rose Goodchild, Daniel Markgraf, Nicolai Karcher, Robin Klemm, Savvas Paragkamian, Sophie Winter and all members of the Schuck lab for comments on the manuscript. This work was supported by a PhD fellowship from the Heidelberg International Graduate School to DP and grant EXC 81 from the Deutsche Forschungsgemeinschaft (DFG, German Research Foundation). BB was funded by projects 319506281 - TRR 186 and 112927078 - TRR 83 from the DFG. The authors declare no competing financial interests.

AUTHOR CONTRIBUTIONS

Conceptualization: Peter Bircham, Dimitrios Papagiannidis, Sebastian Schuck; Formal analysis: Peter Bircham; Investigation: Peter Bircham, Dimitrios Papagiannidis, Christian Lüchtenborg, Giulia Ruffini; Software: Peter Bircham; Supervision: Britta Brügger, Sebastian Schuck; Writing - original draft: Dimitrios Papagiannidis, Sebastian Schuck; Writing - review and editing: all authors.

bioRxiv preprint doi: https://doi.org/10.1101/2020.02.23.961722; this version posted February 24, 2020. The copyright holder for this preprint (which was not certified by peer review) is the author/funder, who has granted bioRxiv a license to display the preprint in perpetuity. It is made available under aCC-BY-NC-ND 4.0 International license.

REFERENCES

Adeyo, O., P.J. Horn, S. Lee, D.D. Binns, A. Chandrahas, K.D. Chapman, and J.M. Goodman. 2011. The yeast lipin orthologue Pah1p is important for biogenesis of lipid droplets. *J Cell Biol*. 192:1043–1055.

Bahmanyar, S., R. Biggs, A.L. Schuh, A. Desai, T. Muller-Reichert, A. Audhya, J.E. Dixon, and K. Oegema. 2014. Spatial control of phospholipid flux restricts endoplasmic reticulum sheet formation to allow nuclear envelope breakdown. *Genes Dev*. 28:121–126.

Bernales, S., K.L. McDonald, and P. Walter. 2006. Autophagy Counterbalances Endoplasmic Reticulum Expansion during the Unfolded Protein Response. *PLoS Biol*. 4:e423.

Bommiasamy, H., S.H. Back, P. Fagone, K. Lee, S. Meshinchi, E. Vink, R. Sriburi, M. Frank, S. Jackowski, R.J. Kaufman, and J.W. Brewer. 2009. ATF6 induces XBP1-independent expansion of the endoplasmic reticulum. *J Cell Sci*. 122:1626–1636.

Campbell, J.L., A. Lorenz, K.L. Witkin, T. Hays, J. Loidl, and O. Cohen-Fix. 2006. Yeast nuclear envelope subdomains with distinct abilities to resist membrane expansion. *Mol Biol Cell*. 17:1768–1778.

Carman, G.M., and G.S. Han. 2019. Fat-regulating phosphatidic acid phosphatases: a review of its roles and regulation in lipid homeostasis. *J Lipid Res*. 60:2–6.

Chen, S., P. Novick, and S. Ferro-Novick. 2012. ER network formation requires a balance of the dynamin-like GTPase Sey1p and the Lunapark family member Lnp1p. *Nat Cell Biol*. 14:707–716.

Costanzo, M., A. Baryshnikova, J. Bellay, Y. Kim, E.D. Spear, C.S. Sevier, H. Ding, J.L.Y. Koh, K. Toufighi, S. Mostafavi, et al. 2010. The genetic landscape of a cell. *Science*. 327:425–431.

Costanzo, M., E. Kuzmin, J. van Leeuwen, B. Mair, J. Moffat, C. Boone, and B. Andrews. 2019. Global Genetic Networks and the Genotype-to-Phenotype Relationship. *Cell*. 177:85–100.

Craddock, C.P., N. Adams, F.M. Bryant, S. Kurup, and P.J. Eastmond. 2015. PHOSPHATIDIC ACID PHOSPHOHYDROLASE Regulates Phosphatidylcholine

bioRxiv preprint doi: https://doi.org/10.1101/2020.02.23.961722; this version posted February 24, 2020. The copyright holder for this preprint (which was not certified by peer review) is the author/funder, who has granted bioRxiv a license to display the preprint in perpetuity. It is made available under aCC-BY-NC-ND 4.0 International license.

807 Biosynthesis in Arabidopsis by Phosphatidic Acid-Mediated Activation of
808 CTP:PHOSPHOCHOLINE CYTIDYLYLTRANSFERASE Activity. *Plant Cell*.
809 27:1251–1264.
810 Davies, A.K., D.N. Itzhak, J.R. Edgar, T.L. Archuleta, J. Hirst, L.P. Jackson, M.S.
811 Robinson, and G.H.H. Borner. 2018. AP-4 vesicles contribute to spatial control
812 ofautophagy via RUSC-dependent peripheraldelivery of ATG9A. *Nat Commun*.
813 9:3958.
814 Dimopoulos, S., C.E. Mayer, F. Rudolf, and J. Stelling. 2014. Accurate cell
815 segmentation in microscopy images using membrane patterns. *Bioinformatics*.
816 30:2644–2651.
817 Dubots, E., S. Cottier, M.P. Péli-Gulli, M. Jaquenoud, S. Bontron, R. Schneiter, and
818 C. De Virgilio. 2014. TORC1 Regulates Pah1 Phosphatidate Phosphatase Activity
819 via the Nem1/Spo7 Protein Phosphatase Complex. *PLoS ONE*. 9:e104194.
820 Eastmond, P.J., A.-L. Quettier, J.T.M. Kroon, C. Craddock, N. Adams, and A.R.
821 Slabas. 2010. PHOSPHATIDIC ACID PHOSPHOHYDROLASE1 and 2 Regulate
822 Phospholipid Synthesis at the Endoplasmic Reticulum in Arabidopsis. *Plant Cell*.
823 22:2796–2811.
824 Ejsing, C.S., J.L. Sampaio, V. Surendranath, E. Duchoslav, K. Ekroos, R.W. Klemm,
825 K. Simons, and A. Shevchenko. 2009. Global analysis of the yeast lipidome by
826 quantitative shotgun mass spectrometry. *Proc Natl Acad Sci USA*. 106:2136–
827 2141.
828 Emmerstorfer, A., M. Wimmer-Teubenbacher, T. Wriessnegger, E. Leitner, M.
829 Müller, I. Kaluzna, M. Schürmann, D. Mink, G. Zellnig, H. Schwab, and H. Pichler.
830 2015. Over-expression of ICE2 stabilizes cytochrome P450 reductase in
831 Saccharomyces cerevisiae and Pichia pastoris. *Biotechnol J*. 10:623–635.
832 Estrada de Martin, P., Y. Du, P. Novick, and S. Ferro-Novick. 2005. Ice2p is
833 important for the distribution and structure of the cortical ER network in
834 Saccharomyces cerevisiae. *J Cell Sci*. 118:65–77.
835 Fanning, S., A. Haque, T. Imberdis, V. Baru, M.I. Barrasa, S. Nuber, D. Termine, N.
836 Ramalingam, G.P.H. Ho, T. Noble, et al. 2019. Lipidomic Analysis of a-Synuclein
837 Neurotoxicity Identifies Stearoyl CoA Desaturase as a Target for Parkinson
838 Treatment. *Mol Cell*. 73:1001–1014.

bioRxiv preprint doi: https://doi.org/10.1101/2020.02.23.961722; this version posted February 24, 2020. The copyright holder for this preprint (which was not certified by peer review) is the author/funder, who has granted bioRxiv a license to display the preprint in perpetuity. It is made available under aCC-BY-NC-ND 4.0 International license.

839 Fawcett, D. 1981. Endoplasmic Reticulum. *In* The Cell. W. B. Saunders,
840 Philadelphia. 303–309.
841 Fei, W., H. Wang, X. Fu, C. Bielby, and H. Yang. 2009. Conditions of endoplasmic
842 reticulum stress stimulate lipid droplet formation in Saccharomyces cerevisiae.
843 *Biochem J*. 424:61–67.
844 Feldheim, D., J. Rothblatt, and R. Schekman. 1992. Topology and functional
845 domains of Sec63p, an endoplasmic reticulum membrane protein required for
846 secretory protein translocation. *Mol Cell Biol*. 12:3288–3296.
847 Giaever, G., A.M. Chu, L. Ni, C. Connelly, L. Riles, S. Véronneau, S. Dow, A. Lucau-
848 Danila, K. Anderson, B. André, et al. 2002. Functional profiling of the
849 Saccharomyces cerevisiae genome. *Nature*. 418:387–391.
850 Golden, A., J. Liu, and O. Cohen-Fix. 2009. Inactivation of the C. elegans lipin
851 homolog leads to ER disorganization and to defects in the breakdown and
852 reassembly of the nuclear envelope. *J Cell Sci*. 122:1970–1978.
853 Grillet, M., B.D. Gonzalez, A. Sicart, M. Pöttler, A. Cascalho, K. Billion, S.H. Diaz, J.
854 Swerts, T.V. Naismith, N.V. Gounko, et al. 2016. Torsins Are Essential Regulators
855 of Cellular Lipid Metabolism. *Dev Cell*. 38:235–247.
856 Gruber, A., D. Hornburg, M. Antonin, N. Krahmer, J. Collado, M. Schaffer, G.
857 Zubaite, C. Lüchtenborg, T. Sachsenheimer, B. Brügger, et al. 2018. Molecular
858 and structural architecture of polyQ aggregates in yeast. *Proc Natl Acad Sci USA*.
859 115:E3446–E3453.
860 Han, G.S., L. O'Hara, G.M. Carman, and S. Siniossoglou. 2008. An unconventional
861 diacylglycerol kinase that regulates phospholipid synthesis and nuclear
862 membrane growth. *J Biol Chem*. 283:20433–20442.
863 Han, G.S., W.I. Wu, and G.M. Carman. 2006. The Saccharomyces cerevisiae Lipin
864 homolog is a Mg2+-dependent phosphatidate phosphatase enzyme. *J Biol Chem*.
865 281:9210–9218.
866 Han, S., S. Bahmanyar, P. Zhang, N. Grishin, K. Oegema, R. Crooke, M. Graham, K.
867 Reue, J.E. Dixon, and J.M. Goodman. 2012. Nuclear envelope phosphatase 1-
868 regulatory subunit 1 (formerly TMEM188) is the metazoan Spo7p ortholog and
869 functions in the lipin activation pathway. *J Biol Chem*. 287:3123–3137.

bioRxiv preprint doi: https://doi.org/10.1101/2020.02.23.961722; this version posted February 24, 2020. The copyright holder for this preprint (which was not certified by peer review) is the author/funder, who has granted bioRxiv a license to display the preprint in perpetuity. It is made available under aCC-BY-NC-ND 4.0 International license.

870 Harris, T.E., and B.N. Finck. 2011. Dual function lipin proteins and glycerolipid
871 metabolism. *Trends Endocrinol Metab*. 22:226–233.
872 Henry, S.A., S.D. Kohlwein, and G.M. Carman. 2012. Metabolism and Regulation of
873 Glycerolipids in the Yeast Saccharomyces cerevisiae. *Genetics*. 190:317–349.
874 Heyken, W.T., A. Repenning, J. Kumme, and H.J. Schüller. 2005. Constitutive
875 expression of yeast phospholipid biosynthetic genes by variants of Ino2 activator
876 defective for interaction with Opi1 repressor. *Mol Microbiol*. 56:696–707.
877 Hu, J., Y. Shibata, P.-P. Zhu, C. Voss, N. Rismanchi, W.A. Prinz, T.A. Rapoport, and
878 C. Blackstone. 2009. A Class of Dynamin-like GTPases Involved in the
879 Generation of the Tubular ER Network. *Cell*. 138:549–561.
880 Inuzuka, M., M. Hayakawa, and T. Ingi. 2005. Serinc, an activity-regulated protein
881 family, incorporates serine into membrane lipid synthesis. *J Biol Chem*.
882 280:35776–35783.
883 Jacquemyn, J., A. Cascalho, and R.E. Goodchild. 2017. The ins and outs of
884 endoplasmic reticulum-controlled lipid biosynthesis. *EMBO Rep*. 18:1905–1921.
885 James, A.W., R. Gowsalya, and V. Nachiappan. 2016. Dolichyl pyrophosphate
886 phosphatase-mediated N -glycosylation defect dysregulates lipid homeostasis in
887 Saccharomyces cerevisiae. *Biochim Biophys Acta*. 1861:1705–1718.
888 James, A.W., C. Ravi, M. Srinivasan, and V. Nachiappan. 2019. Crosstalk between
889 protein N-glycosylation and lipid metabolism in Saccharomyces cerevisiae. *Sci*
890 *Rep*. 9:14485.
891 Janke, C., M.M. Magiera, N. Rathfelder, C. Taxis, S. Reber, H. Maekawa, A.
892 Moreno-Borchart, G. Doenges, E. Schwob, E. Schiebel, and M. Knop. 2004. A
893 versatile toolbox for PCR-based tagging of yeast genes: new fluorescent proteins,
894 more markers and promoter substitution cassettes. *Yeast*. 21:947–962.
895 Jonikas, M.C., S.R. Collins, V. Denic, E. Oh, E.M. Quan, V. Schmid, J. Weibezahn,
896 B. Schwappach, P. Walter, J.S. Weissman, and M. Schuldiner. 2009.
897 Comprehensive characterization of genes required for protein folding in the
898 endoplasmic reticulum. *Science*. 323:1693–1697.
899 Karanasios, E., G.S. Han, Z. Xu, G.M. Carman, and S. Siniossoglou. 2010. A
900 phosphorylation-regulated amphipathic helix controls the membrane translocation

bioRxiv preprint doi: https://doi.org/10.1101/2020.02.23.961722; this version posted February 24, 2020. The copyright holder for this preprint (which was not certified by peer review) is the author/funder, who has granted bioRxiv a license to display the preprint in perpetuity. It is made available under aCC-BY-NC-ND 4.0 International license.

and function of the yeast phosphatidate phosphatase. *Proc Natl Acad Sci USA*. 107:17539–17544.

Kushnirov, V.V. 2000. Rapid and reliable protein extraction from yeast. *Yeast*. 16:857–860.

Kwiatek, J.M., G.S. Han, and G.M. Carman. 2020. Phosphatidate-mediated regulation of lipid synthesis at the nuclear/endoplasmic reticulum membrane. *Biochim Biophys Acta*.

Loewen, C.J.R., M.L. Gaspar, S.A. Jesch, C. Delon, N.T. Ktistakis, S.A. Henry, and T.P. Levine. 2004. Phospholipid metabolism regulated by a transcription factor sensing phosphatidic acid. *Science*. 304:1644–1647.

Longtine, M.S., A. McKenzie, D.J. Demarini, N.G. Shah, A. Wach, A. Brachat, P. Philippsen, and J.R. Pringle. 1998. Additional modules for versatile and economical PCR-based gene deletion and modification in Saccharomyces cerevisiae. *Yeast*. 14:953–961.

Markgraf, D.F., R.W. Klemm, M. Junker, H.K. Hannibal-Bach, C.S. Ejsing, and T.A. Rapoport. 2014. An ER Protein Functionally Couples Neutral Lipid Metabolism on Lipid Droplets to Membrane Lipid Synthesis in the ER. *Cell Rep*. 6:44–55.

McMaster, C.R. 2018. From yeast to humans – roles of the Kennedy pathway for phosphatidylcholine synthesis. *FEBS Lett*. 592:1256–1272.

Mumberg, D., R. Müller, and M. Funk. 1994. Regulatable promoters of Saccharomyces cerevisiae: comparison of transcriptional activity and their use for heterologous expression. *Nucleic Acids Res*. 22:5767–5768.

Mumberg, D., R. Müller, and M. Funk. 1995. Yeast vectors for the controlled expression of heterologous proteins in different genetic backgrounds. *Gene*. 156:119–122.

Nagy, Z., S. Comer, and A. Smolenski. 2018. Analysis of Protein Phosphorylation Using Phos-Tag Gels. Curr Protoc Protein Sci. 93:e64.

Nixon-Abell, J., C.J. Obara, A.V. Weigel, D. Li, W.R. Legant, C.S. Xu, H.A. Pasolli, K. Harvey, H.F. Hess, E. Betzig, et al. 2016. Increased spatiotemporal resolution reveals highly dynamic dense tubular matrices in the peripheral ER. *Science*. 354:aaf3928.

bioRxiv preprint doi: https://doi.org/10.1101/2020.02.23.961722; this version posted February 24, 2020. The copyright holder for this preprint (which was not certified by peer review) is the author/funder, who has granted bioRxiv a license to display the preprint in perpetuity. It is made available under aCC-BY-NC-ND 4.0 International license.

O'Hara, L., G.S. Han, S. Peak-Chew, N. Grimsey, G.M. Carman, and S. Siniossoglou. 2006. Control of phospholipid synthesis by phosphorylation of the yeast lipin Pah1p/Smp2p Mg2+-dependent phosphatidate phosphatase. *J Biol Chem*. 281:34537–34548.

Özbalci, C., T. Sachsenheimer, and B. Brügger. 2013. Quantitative Analysis of Cellular Lipids by Nano-Electrospray Ionization Mass Spectrometry. *In* Methods in Molecular Biology. Humana Press, Totowa, NJ. 3–20.

Pillai, A.N., S. Shukla, and A. Rahaman. 2017. An evolutionarily conserved phosphatidate phosphatase maintains lipid droplet number and endoplasmic reticulum morphology but not nuclear morphology. *Biol Open*. 6:1629–1643.

Pincus, D., A. Aranda-Diaz, I.A. Zuleta, P. Walter, and H. El-Samad. 2014. Delayed Ras/PKA signaling augments the unfolded protein response. *Proc Natl Acad Sci USA*. 111:14800–14805.

Pincus, D., M.W. Chevalier, T. Aragón, E. van Anken, S.E. Vidal, H. El-Samad, and P. Walter. 2010. BiP Binding to the ER-Stress Sensor Ire1 Tunes the Homeostatic Behavior of the Unfolded Protein Response. *PLoS Biol*. 8:e1000415.

Puhka, M., M. Joensuu, H. Vihinen, I. Belevich, and E. Jokitalo. 2012. Progressive sheet-to-tubule transformation is a general mechanism for endoplasmic reticulum partitioning in dividing mammalian cells. *Mol Biol Cell*. 23:2424–2432.

Rosa, A., A. Chande, S. Ziglio, V. De Sanctis, R. Bertorelli, S.L. Goh, S.M. McCauley, A. Nowosielska, S.E. Antonarakis, J. Luban, F.A. Santoni, and M. Pizzato. 2015. HIV-1 Nef promotes infection by excluding SERINC5 from virion incorporation. *Nature*. 526:212–217.

Sandager, L., M.H. Gustavsson, U. Ståhl, A. Dahlqvist, E. Wiberg, A. Banas, M. Lenman, H. Ronne, and S. Stymne. 2002. Storage Lipid Synthesis Is Non-essential in Yeast. *J Biol Chem*. 277:6478–6482.

Santos-Rosa, H., J. Leung, N. Grimsey, S. Peak-Chew, and S. Siniossoglou. 2005. The yeast lipin Smp2 couples phospholipid biosynthesis to nuclear membrane growth. *EMBO J*. 24:1931–1941.

Schäfer, J.A., J.P. Schessner, P.W. Bircham, T. Tsuji, C. Funaya, O. Pajonk, K. Schaeff, G. Ruffini, D. Papagiannidis, M. Knop, et al. 2020. ESCRT machinery mediates selective microautophagy of endoplasmic reticulum in yeast. *EMBO J*.

bioRxiv preprint doi: https://doi.org/10.1101/2020.02.23.961722; this version posted February 24, 2020. The copyright holder for this preprint (which was not certified by peer review) is the author/funder, who has granted bioRxiv a license to display the preprint in perpetuity. It is made available under aCC-BY-NC-ND 4.0 International license.

964 Schmidt, R.M., J.P. Schessner, G.H. Borner, and S. Schuck. 2019. The proteasome
965 biogenesis regulator Rpn4 cooperates with the unfolded protein response to
966 promote ER stress resistance. *eLife*. 8:e43244.
967 Schroeder, L.K., A.E.S. Barentine, H. Merta, S. Schweighofer, Y. Zhang, D.
968 Baddeley, J. Bewersdorf, and S. Bahmanyar. 2019. Dynamic nanoscale
969 morphology of the ER surveyed by STED microscopy. *J Cell Biol*. 218:83–96.
970 Schuck, S., W.A. Prinz, K.S. Thorn, C. Voss, and P. Walter. 2009. Membrane
971 expansion alleviates endoplasmic reticulum stress independently of the unfolded
972 protein response. *J Cell Biol*. 187:525–536.
973 Schuldiner, M., S.R. Collins, N.J. Thompson, V. Denic, A. Bhamidipati, T. Punna, J.
974 Ihmels, B. Andrews, C. Boone, J.F. Greenblatt, et al. 2005. Exploration of the
975 Function and Organization of the Yeast Early Secretory Pathway through an
976 Epistatic Miniarray Profile. *Cell*. 123:507–519.
977 Shaner, N.C., G.G. Lambert, A. Chammas, Y. Ni, P.J. Cranfill, M.A. Baird, B.R. Sell,
978 J.R. Allen, R.N. Day, M. Israelsson, et al. 2013. A bright monomeric green
979 fluorescent protein derived from Branchiostoma lanceolatum. *Nat Methods*.
980 10:407–409.
981 Shibata, Y., T. Shemesh, W.A. Prinz, A.F. Palazzo, M.M. Kozlov, and T.A. Rapoport.
982 2010. Mechanisms Determining the Morphology of the Peripheral ER. *Cell*.
983 143:774–788.
984 Sidrauski, C., J.S. Cox, and P. Walter. 1996. tRNA ligase is required for regulated
985 mRNA splicing in the unfolded protein response. *Cell*. 87:405-413.
986 Siniossoglou, S., H. Santos-Rosa, J. Rappsilber, M. Mann, and E. Hurt. 1998. A
987 novel complex of membrane proteins required for formation of a spherical
988 nucleus. *EMBO J*. 17:6449–6464.
989 Sprouffske, K, and A. Wagner. 2016. Growthcurver: an R package for obtaining
990 interpretable metrics from microbial growthcurves. *BMC Bioinformatics*. 17:172.
991 Sriburi, R., H. Bommiasamy, G.L. Buldak, G.R. Robbins, M. Frank, S. Jackowski,
992 and J.W. Brewer. 2007. Coordinate regulation of phospholipid biosynthesis and
993 secretory pathway gene expression in XBP-1(S)-induced endoplasmic reticulum
994 biogenesis. *J Biol Chem*. 282:7024–7034.

bioRxiv preprint doi: https://doi.org/10.1101/2020.02.23.961722; this version posted February 24, 2020. The copyright holder for this preprint (which was not certified by peer review) is the author/funder, who has granted bioRxiv a license to display the preprint in perpetuity. It is made available under aCC-BY-NC-ND 4.0 International license.

995 Su, W.-M., G.-S. Han, J. Casciano, and G.M. Carman. 2012. Protein kinase A-
996 mediated phosphorylation of Pah1p phosphatidate phosphatase functions in
997 conjunction with the Pho85p-Pho80p and Cdc28p-cyclin B kinases to regulate
998 lipid synthesis in yeast. *J Biol Chem*. 287:33364–33376.
999 Surma, M.A., C. Klose, D. Peng, M. Shales, C. Mrejen, A. Stefanko, H. Braberg, D.E.
1000 Gordon, D. Vorkel, C.S. Ejsing, et al. 2013. A Lipid E-MAP Identifies Ubx2 as a
1001 Critical Regulator of Lipid Saturation and Lipid Bilayer Stress. *Mol Cell*. 51:519–
1002 530.
1003 Szoradi, T., K. Schaeff, E.M. Garcia-Rivera, D.N. Itzhak, R.M. Schmidt, P.W.
1004 Bircham, K. Leiss, J. Diaz-Miyar, V.K. Chen, D. Muzzey, et al. 2018. SHRED Is a
1005 Regulatory Cascade that Reprograms Ubr1 Substrate Specificity for Enhanced
1006 Protein Quality Control during Stress. *Mol Cell*. 70:1025–1037.
1007 Tarassov, K., V. Messier, C.R. Landry, S. Radinovic, M.M. Serna Molina, I. Shames,
1008 Y. Malitskaya, J. Vogel, H. Bussey, and S.W. Michnick. 2008. An in vivo map of
1009 the yeast protein interactome. *Science*. 320:1465–1470.
1010 Tavassoli, S., J.T. Chao, B.P. Young, R.C. Cox, W.A. Prinz, A.I.P.M. de Kroon, and
1011 C.J.R. Loewen. 2013. Plasma membrane-endoplasmic reticulum contact sites
1012 regulate phosphatidylcholine synthesis. *EMBO Rep*. 14:434–440.
1013 Tkach, J.M., A. Yimit, A.Y. Lee, M. Riffle, M. Costanzo, D. Jaschob, J.A. Hendry, J.
1014 Ou, J. Moffat, C. Boone, et al. 2012. Dissecting DNA damage response pathways
1015 by analysing protein localization and abundance changes during DNA replication
1016 stress. *Nat Cell Biol*. 14:966–976.
1017 Tong, A.H.Y., and C. Boone. 2007. High-Throughput Strain Construction and
1018 Systematic Synthetic Lethal Screening in Saccharomyces cerevisiae. *In* Methods
1019 in Microbiology. Elsevier. 36:369–386.
1020 Velázquez, A.P., T. Tatsuta, R. Ghillebert, I. Drescher, and M. Graef. 2016. Lipid
1021 droplet–mediated ER homeostasis regulates autophagy and cell survival during
1022 starvation. *J Cell Biol*. 212:621–631.
1023 Wagih, O., and L. Parts. 2014. gitter: A Robust and Accurate Method for
1024 Quantification of Colony Sizes From Plate Images. *G3 (Bethesda)*. 4:547–552.
1025 Walter, P., and D. Ron. 2011. The unfolded protein response: from stress pathway to
1026 homeostatic regulation. *Science*. 334:1081–1086.

bioRxiv preprint doi: https://doi.org/10.1101/2020.02.23.961722; this version posted February 24, 2020. The copyright holder for this preprint (which was not certified by peer review) is the author/funder, who has granted bioRxiv a license to display the preprint in perpetuity. It is made available under aCC-BY-NC-ND 4.0 International license.

West, M., N. Zurek, A. Hoenger, and G.K. Voeltz. 2011. A 3D analysis of yeast ER structure reveals how ER domains are organized by membrane curvature. *J Cell Biol*. 193:333–346.

Westrate, L.M., J.E. Lee, W.A. Prinz, and G.K. Voeltz. 2015. Form Follows Function: The Importance of Endoplasmic Reticulum Shape. *Annu Rev Biochem.* 84:791–811.

Wiest, D.L., J.K. Burkhardt, S. Hester, M. Hortsch, D.I. Meyer, and Y. Argon. 1990. Membrane biogenesis during B cell differentiation: most endoplasmic reticulum proteins are expressed coordinately. *J Cell Biol*. 110:1501–1511.

Yang, C., X. Wang, J. Wang, X. Wang, W. Chen, N. Lu, S. Siniossoglou, Z. Yao, and K. Liu. 2019. Rewiring Neuronal Glycerolipid Metabolism Determines the Extent of Axon Regeneration. *Neuron*.

Zhang, P., and K. Reue. 2017. Lipin proteins and glycerolipid metabolism: Roles at the ER membrane and beyond. *Biochim Biophys Acta*. 1859:1583–1595.

Zhang, P., L.S. Csaki, E. Ronquillo, L.J. Baufeld, J.Y. Lin, A. Gutierrez, J.R. Dwyer, D.N. Brindley, L.G. Fong, P. Tontonoz, et al. 2019. Lipin 2/3 phosphatidic acid phosphatases maintain phospholipid homeostasis to regulate chylomicron synthesis. *J Clin Invest*. 129:281–295.

Zhang, P., M.A. Verity, and K. Reue. 2014. Lipin-1 Regulates Autophagy Clearance and Intersects with Statin Drug Effects in Skeletal Muscle. *Cell Metab*. 20:267–279.

bioRxiv preprint doi: https://doi.org/10.1101/2020.02.23.961722; this version posted February 24, 2020. The copyright holder for this preprint (which was not certified by peer review) is the author/funder, who has granted bioRxiv a license to display the preprint in perpetuity. It is made available under aCC-BY-NC-ND 4.0 International license.

FIGURE LEGENDS

Figure 1. An inducible system for ER membrane biogenesis. **(A)** Schematic of the control of lipid synthesis by estradiol-inducible expression of ino2*. **(B)** Sec63-mNeon images of mid and cortical sections of cells harboring the estradiol-inducible system (SSY1405). Cells were untreated or treated with 800 nM estradiol for 6 h. Estradiol induces expansion of the peripheral ER. **(C)** Flow cytometric measurement of GFP levels in cells containing the UPR reporter. WT cells containing the UPR reporter (SSY2306), cells additionally harboring an estradiol-inducible *GAL* promoter (SSY2307) and cells additionally harboring the system for estradiol-inducible expression of ino2* under the *GAL* promoter (SSY2308) were untreated, treated with 800 nM estradiol for 6 h or treated with 8 mM DTT for 1 h, as indicated. Data are normalized to untreated wild-type cells. Mean ± SEM, n = 3. WT, wild-type. **(D)** Western blot of Sec63, mCherry and Pgk1 from WT cells (SSY1404), cells harboring the estradiol-inducible system (SSY1405) or *Δopi1* cells (SSY1607), all of which expressed Sec63-mNeon and Rtn1-mCherry. Cells were untreated or treated with 800 nM estradiol for 6 h. Pgk1 served as a loading control. **(E)** Quantification of ER size in estradiol-treated cells harboring the inducible system (SSY1405), untreated *Δopi1* cells (SSY1607) and WT cells (SSY1404) treated with 8 mM DTT for 1 h. The three metrics for the size of the peripheral ER at the cell cortex show dose-dependent ER expansion upon estradiol treatment, reaching the constitutive expansion in *Δopi1* cells. Mean ± SEM, n = 3.

Figure 2. A genetic screen for factors involved in ER membrane biogenesis. **(A)** Sec63-mNeon images of cells of the indicated genotypes harboring the inducible system. Cells were treated with 800 nM estradiol for 6 h. Two examples of each phenotypic class are shown. WT, wild-type. **(B)** Violin plots of Z scores from the three metrics for ER size determined for each of the 4800 mutants strains in the yeast knockout collection. The untreated WT is shown for reference. **(C)** Sec63-mNeon and Rtn1-mCherry images of *Δlnp1* and *Δsey1* cells harboring the inducible system and treated with 800 nM estradiol for 6 h. **(D)** Classification of hits. Numbers

bioRxiv preprint doi: https://doi.org/10.1101/2020.02.23.961722; this version posted February 24, 2020. The copyright holder for this preprint (which was not certified by peer review) is the author/funder, who has granted bioRxiv a license to display the preprint in perpetuity. It is made available under aCC-BY-NC-ND 4.0 International license.

in brackets indicate the number of mutants in each class. Striped areas indicate mutants falling into two classes.

Figure 3. Ice2 is required for ER membrane biogenesis upon activation of Ino2/4. **(A)** Sec63-mNeon images of the cortical ER of WT and *Δice2* cells harboring the inducible system (SSY1405 and 1603). Cells were untreated or treated with 800 nM estradiol for 6 h. WT, wild-type. **(B)** Classification of peripheral ER structures from cortical sections of cells expressing Sec63-mNeon and Rtn1-mCherry as tubules (purple), sheets (green) or tubular clusters (yellow). Tubular clusters are added to the tubules in the final classification, as illustrated by the overlay. **(C)** Quantification of peripheral ER structures in WT and *Δice2* cells harboring the inducible system (SSY1405 and 1603) and treated with 800 nM estradiol for the times indicated. Plotted is the percentage of cell cortex covered by tubules (purple) or sheets (green). Error bars show the SEM for tubules and sheets, respectively. n = 3. ER expansion is driven by sheet formation, which fails in *Δice2* cells. **(D)** Activity of the Ino2/4 target gene *INO1* before and after ino2* expression in WT and *Δice2* cells harboring the inducible system (SSY1405 and 1603) as judged by mRNA levels measured by quantitative real-time PCR. Data are normalized to untreated WT cells. Mean ± SEM. n = 3. **(E)** Quantification of peripheral ER structures in untreated WT, *Δice2*, *Δopi1* and *Δice2 Δopi1* cells (SSY1404, 2356, 2595 and 2811). Deletion of *ICE2* impaires ER expansion caused by deletion of *OPI1*.

Figure 4. Ice2 is required for ER membrane biogenesis upon ER stress and *ICE2* overexpression is sufficient to induce ER expansion. **(A)** Quantification of peripheral ER structures in WT and *Δice2* cells (SSY1405 and 1603) treated with 8 mM DTT for the times indicated. Plotted is the percentage of cell cortex covered by tubules (purple) or sheets (green). Error bars show the SEM for tubules and sheets, respectively. n = 3. WT, wild-type. **(B)** Flow cytometric measurement of GFP levels of WT and *Δice2* cells containing the UPR reporter (SSY2306 and 2312). Cells were treated with 8 mM DTT for the times indicated. Data are normalized to untreated WT cells. Mean ± SEM, n = 3. **(C)** Fluorescence images of cortical sections of untreated WT and *Δice2* cells expressing Sec63-mNeon and Rtn1-mCherry (SSY1405 and

bioRxiv preprint doi: https://doi.org/10.1101/2020.02.23.961722; this version posted February 24, 2020. The copyright holder for this preprint (which was not certified by peer review) is the author/funder, who has granted bioRxiv a license to display the preprint in perpetuity. It is made available under aCC-BY-NC-ND 4.0 International license.

1603). **(D)** As in panel C, but after treatment with 8 mM DTT for 1 h. **(E)** Quantification of WT and *Δice2* cells with Rtn1-mCherry puncta after treatment with 8 mM DTT for the times indicated. Mean ± SEM. n = 3. **(F)** Quantification of peripheral ER structures in untreated WT and UPR-deficient *Δhac1* cells (SSY2228 and 2331), overexpressing *ICE2* from a centromeric plasmid where indicated. **(G)** Flow cytometric measurement of GFP levels of WT and *Δhac1* cells containing the UPR reporter (SSY2306 and 2314) and overexpressing *ICE2* from a centromeric plasmid where indicated. Data are normalized to untreated WT cells. Mean ± SEM, n = 3.

Figure 5. Ice2 cooperates with Nem1, Spo7 and Pah1. **(A)** Quantification of peripheral ER structures in WT, *Δice2*, *ΔLD* and *ΔLD Δice2* cells harboring the inducible system (SSY2598, 599, 2600 and 2601), which were untreated or treated with 800 nM estradiol for 6 h. Plotted is the percentage of cell cortex covered by tubules (purple) or sheets (green). Error bars show the SEM for tubules and sheets, respectively. n = 3. WT, wild-type; *ΔLD*, *Δlipid droplet*. The absence of lipid droplets has no effect on ER expansion or the expansion defect caused by deletion of *ICE2*. **(B)** As in panel A but after treatment with 8 mM DTT for 1 h. **(C)** Principle of the Ice2 protein proximity screen (left) and table of the hits obtained (right). DHFR*$_N$ and DHFR*$_C$ are the amino-terminal and carboxy-terminal fragments of methotrexate-resistant dihydrofolate reductase. **(D)** Genetic interactions between *ICE2* and selected lipid synthesis genes. CDP, cytidine diphosphate; DAG, diacylglycerol; PA, phosphatidic acid; PI/PS/PE/PC, phosphatidyl-inositol/serine/ethanolamine/choline. **(E)** Growth assays of untreated WT, *Δice2*, *Δpah1* and *Δpah1Δice2* cells (SSY1404, 2356, 2807 and 2808). Numbers represent the areas under the curves and serve as growth indices. Mean ± SEM. n = 3. Deletion of *PAH1* suppresses the growth phenotype caused by deletion of *ICE2*. **(F)** Fluorescence images of WT, *Δpah1* and *Δpah1Δice2* cells expressing Sec63-mNeon (SSY1404, 2807 and 2808). *ICE2* deletion has no effect on nuclear or peripheral ER morphology in *Δpah1* cells.

Figure 6. Ice2 promotes ER membrane biogenesis by opposing Pah1 activity. **(A)** Schematic of Pah1 phospho-regulation. Phosphorylated Pah1 is cytosolic and inactive. Interaction between Pah1 and the ER-localized Nem1-Spo7 complex

bioRxiv preprint doi: https://doi.org/10.1101/2020.02.23.961722; this version posted February 24, 2020. The copyright holder for this preprint (which was not certified by peer review) is the author/funder, who has granted bioRxiv a license to display the preprint in perpetuity. It is made available under aCC-BY-NC-ND 4.0 International license.

results in Pah1 dephosphorylation and activation, leading to conversion of PA into DAG. **(B)** Western blot of HA from WT, *Δice2*, *Δnem1* and *Δnem1 Δice2* cells expressing endogenously tagged Pah1-3HA (SSY2592, 2593, 2595 and 2718). SDS-PAGE (top) and Phos-tag PAGE (bottom) gels are shown. WT, wild-type. Loss of Ice2 results in dephosphorylation and hence activation of Pah1 by Nem1, indicating that Ice2 opposes Pah1 activity. **(C)** Lipidomic analysis of WT, *Δice2*, *Δnem1* and *Δice2 Δnem1* cells (SSY1404, 2356, 2482 and 2484). Mean ± SEM. n = 4. TAG, triacylglycerol; DAG, diacylglycerol; PA, phosphatidic acid; PI/PS/PE/PC, phosphatidyl-inositol/serine/ethanolamine/choline. **(D)** As in panel C, but of WT, *Δice2*, *Δspo7* and *Δice2 Δspo7* cells (SSY1404, 2356, 2481 and 2483). Data for WT and *Δice2* cells are the same as in panel C. **(E)** Quantification of peripheral ER structures in WT cells and cells in which *PAH1* was replaced by *pah1(7A)*, without and with overexpression of *ICE2* (SSY2841, 2842, 2843 and 2844). Plotted is the percentage of cell cortex covered by tubules (purple) or sheets (green). Error bars show the SEM for tubules and sheets, respectively. n = 3. The constitutively active *pah1(7A)* prevents ER membrane expansion upon *ICE2* overexpression. **(F)** Quantification of peripheral ER structures in WT cells and cells in which *PAH1* was replaced by *pah1(7A)* (SSY2841 and 2842), treated with 8 mM DTT for 1 h. **(G)** Quantification of WT and *Δice2* cells with Rtn1-mCherry puncta after treatment with 8 mM DTT for the times indicated. Mean ± SEM. n = 3.

Figure 7. Ice2 cooperates with the PA-Opi1-Ino2/4 system and the UPR. **(A)** Sec63-mNeon images of mid and cortical sections of untreated WT and *Δopi1* cells, overexpressing *ICE2* where indicated (SSY1404, 2595, 2588 and 2596). WT, wild-type. **(B)** Quantification of peripheral ER structures in the strains shown in panel A. Plotted is the percentage of cell cortex covered by tubules (purple) or sheets (green). Error bars show the SEM for tubules and sheets, respectively. n = 3. **(C)** Growth assays of untreated WT, *Δhac1*, *Δice2*, and *Δhac1Δice2* cells (SSY1404, 2356, 2805 and 2806). Numbers represent the areas under the curves and serve as growth indices. Mean ± SEM. n = 3. **(D)** Model for the regulation of ER membrane biogenesis. High Pah1 activity promotes conversion of phosphatidic acid (PA) into diacylglycerol (DAG) for lipid droplet biogenesis. Low Pah1 activity allows net DAG-

bioRxiv preprint doi: https://doi.org/10.1101/2020.02.23.961722; this version posted February 24, 2020. The copyright holder for this preprint (which was not certified by peer review) is the author/funder, who has granted bioRxiv a license to display the preprint in perpetuity. It is made available under aCC-BY-NC-ND 4.0 International license.

to-PA conversion by Dgk1 and derepression of Ino2/4-driven lipid synthesis genes, resulting in phospholipid production and ER membrane biogenesis. These mechanisms coordinate the production of lipid metabolic precursors and lipid synthesis enzymes.

Figure S1. (A) Growth assays of untreated WT, *Δice2*, *ΔLD* and *ΔLD Δice2* cells (SSY2228, 2229, 2230 and 2256). Numbers represent the areas under the curves and serve as growth indices. WT, wild-type. Mean ± SEM. n = 3. *ΔLD*, *Δlipid droplet*. The absence of lipid droplets has no effect on ER expansion or the expansion defect caused by deletion of *ICE2*. **(B)** Growth assay of untreated S288C WT cells mating type a or alpha, the corresponding cells harboring Ice2 fused to either fragment of DHFR*, and *Δice2* cells. Numbers represent the areas under the curves and serve as growth indices. n = 1. Ice2-DHFR fusion proteins support normal growth, indicating that they are functional.

Figure S2. Ice2 but not Dgk1 acts in the same pathway as Nem1, Spo7 and Pah1. **(A)** Growth assays of untreated WT, *Δice2*, *Δnem1* and *Δnem1Δice2* cells (SSY1404, 2356, 2482 and 2484). Numbers represent the areas under the curves and serve as growth indices. Mean ± SEM. n = 3. WT, wild-type. Deletion of *NEM1* suppresses the growth phenotype caused by deletion of *ICE2*. **(B)** Sec63-mNeon images of untreated WT, *Δice2*, *Δnem1* and *Δnem1Δice2* cells (SSY1404, 2356, 2482 and 2484). *ICE2* deletion has no effect on nuclear or peripheral ER morphology in *Δnem1* cells. **(C)** As in panel A but for WT, *Δice2*, *Δspo7* and *Δspo7Δice2* cells (SSY1404, 2356, 2481 and 2483). Data for WT and *Δice2* cells are the same as in panel A. **(D)** As in panel B but for WT, *Δice2*, *Δspo7* and *Δspo7Δice2* cells (SSY1404, 2356, 2481 and 2483). **(E)** Sec63-mNeon images of untreated cells of the indicated genotypes (SSY1404, 2482, 2481, 2807, 2480, 2485, 2486 and 2822). *DGK1* deletion rescues the nuclear envelope defects and constitutive ER expansion in *Δnem1*, *Δspo7* and *Δpah1* cells.

bioRxiv preprint doi: https://doi.org/10.1101/2020.02.23.961722; this version posted February 24, 2020. The copyright holder for this preprint (which was not certified by peer review) is the author/funder, who has granted bioRxiv a license to display the preprint in perpetuity. It is made available under aCC-BY-NC-ND 4.0 International license.

Table S3. Plasmids used in this study. GEM = GAL4DBD-EstR-Msn2TAD.

Plasmid	Alias	Source
pRS415-P_{MET25}-ino2(L119A)	pSS108	Heyken et al., 2005
pRS416-P_{GAL1}	pSS031	Mumberg et al., 1994
pRS415-P_{GAL1}-ino2(L119A)	pSS448	this study
pNH605-P_{ADH1}-GEM	pDEP151	David Pincus
pNH605-P_{ADH1}-GEM-P_{GAL1}	pSS474	Schmidt et al., 2019
pNH605-P_{ADH1}-GEM-P_{GAL1}-ino2(L119A)	pSS475	this study
pRS306-P_{ADH1}-GEM	pDEP001	Pincus et al., 2014
pRS306-P_{ADH1}-GEM-P_{GAL1}	pSS476	Schmidt et al., 2019
pRS306-P_{ADH1}-GEM-P_{GAL1}-ino2(L119A)	pSS477	this study
pRS303H-P_{GPD}-TagBFP	pMaM245	Szoradi et al., 2018
pFA6a-mNeon-kanMX4	pMaM375	Michael Knop
pFA6a-GFP(S65T)-kanMX6	pSS037	Longtine et al., 1998
pFA6a-GFP(S65T)-HISMX6	pSS039	Longtine et al., 1998
pFA6a-mNeon-kanMX6	pSS445	Schäfer et al., 2020
pFA6a-mNeon-HIS3MX6	pSS447	this study
pRS415-P_{ADH1}	pSS022	Mumberg et al., 1995
pRS415-P_{ADH1}-Ice2	pSS761	this study
pRS304-4xUPRE-GFP	pDEP017	Pincus et al., 2010
YCplac111-Pah1-PrtA	pSS1005	O'Hara et al., 2006
YCplac111-pah1(7A)-PrtA	pSS1006	O'Hara et al., 2006
YCplac111-Pah1-3HA	pSS1045	this study
YCplac111-pah1(7A)-3HA	pSS1047	this study

bioRxiv preprint doi: https://doi.org/10.1101/2020.02.23.961722; this version posted February 24, 2020. The copyright holder for this preprint (which was not certified by peer review) is the author/funder, who has granted bioRxiv a license to display the preprint in perpetuity. It is made available under aCC-BY-NC-ND 4.0 International license.

Table S4. Yeast strains used in this study. mNeon = mNeonGreen. GEM = P_{ADH1}-GAL4DBD-EstR-Msn2TAD.

Strain	Relevant genotype	Source
SSY122	*ADE2 leu2-3,112 trp1-1 ura3-1 his3-11,15 MATa*	Szoradi, 2018
SSY1404	*Sec63-mNeon::kan Rtn1-mCherry::HIS3*	this study
SSY2328	*Sec63-mNeon::kan Rtn1-mCherry::HIS3 leu2::GEM-LEU2*	this study
SSY1405	*Sec63-mNeon::kan Rtn1-mCherry::HIS3 leu2::GEM-P_{GAL1}-ino2(L119A)-LEU2*	this study
SSY2306	*his3::P_{GPD}-TagBFP-hph trp1::4xUPRE-GFP-TRP1*	this study
SSY2307	*his3::P_{GPD}-TagBFP-hph trp1::4xUPRE-GFP-TRP1 ura3::GEM-P_{GAL1}-URA3*	this study
SSY2308	*his3::P_{GPD}-TagBFP-hph trp1::4xUPRE-GFP-TRP1 ura3::GEM-P_{GAL1}-ino2(L119A)-URA3*	this study
SSY1607	*Sec63-mNeon::kan Rtn1-mCherry::HIS3 leu2::GEM-P_{GAL1}-ino2(L119A)-LEU2 opi1Δ::hph*	this study
Y8205	*can1Δ::P_{STE2}-Sp_his5 lyp1Δ::P_{STE3}-LEU2 his3Δ1 leu2Δ0 ura3Δ0 MATα*	Tong, 2007
SSY2589	*Y8205 Sec63-mNeon::HIS3 his3::P_{GPD}-TagBFP-hph can1::GEM-P_{GAL1}-ino2(L119A)-URA3*	this study
SSY2590	*Y8205 Rtn1-mCherry::nat lyp1::GEM-P_{GAL1}-ino2(L119A)-URA3*	this study
SSY1603	*Sec63-mNeon::kan Rtn1-mCherry::HIS3 leu2::GEM-P_{GAL1}-ino2(L119A)-LEU2 ice2Δ::hph*	this study
SSY2356	*Sec63-mNeon::kan Rtn1-mCherry::HIS3 ice2Δ::nat*	this study
SSY2595	*Sec63-mNeon::kan Rtn1-mCherry::HIS3 opi1Δ::hph*	this study
SSY2811	*Sec63-mNeon::kan Rtn1-mCherry::HIS3 opi1Δ::hph ice2Δ::nat*	this study
SSY2312	*his3::P_{GPD}-TagBFP-hph trp1::4xUPRE-GFP-TRP1 ice2Δ::nat*	this study
YMG1	*ade2-1 leu2-3,112 trp1-1 ura3-1 his3-11,15 can1-100 MATa*	Velazquez, 2016
SSY2228	*YMG1 Sec63-mNeon::URA3 Rtn1-mCherry::kan*	this study
SSY2331	*YMG1 Sec63-mNeon::URA3 Rtn1-mCherry::kan hac1Δ::nat*	this study
SSY2314	*his3::P_{GPD}-TagBFP-hph trp1::4xUPRE-GFP-TRP1 hac1Δ::nat*	this study
YMG5	*YMG1 dga1Δ::TRP1 lro1Δ::HIS3 are1Δ::TRP1 are2Δ::HIS3*	Velazquez, 2016
SSY2598	*YMG1 ADE2 Sec63-mNeon::URA3 Rtn1-mCherry::kan leu2::GEM-P_{GAL1}-ino2(L119A)-LEU2*	this study
SSY2599	*SSY2598 ice2Δ::nat*	this study
SSY2600	*YMG5 ADE2 Sec63-mNeon::URA3 Rtn1-mCherry::kan leu2::GEM-P_{GAL1}-ino2(L119A)-LEU2*	this study
SSY2601	*SSY2600 ice2Δ::nat*	this study
BY4741	*his3Δ1 leu2Δ0 met15Δ0 ura3Δ0 MATa*	Michael Knop
BY4742	*his3Δ1 leu2Δ0 leu2Δ0 ura3Δ0 MATα*	Michael Knop
	BY4741 Ice2-DHFR$_{1,2}$ (from DHFR fusion collection)*	Tarassov, 2008
	BY4742 Ice2-DHFR$_{3}$ (from DHFR fusion collection)*	Tarassov, 2008
	BY4741 Hmg2-DHFR$_{1,2}$ (from DHFR fusion collection)*	Tarassov, 2008
	BY4742 Hmg2-DHFR$_{3}$ (from DHFR fusion collection)*	Tarassov, 2008
	BY4741 ice2Δ::kan (from knockout strain collection)	Giaever, 2002
SSY2807	*Sec63-mNeon::kan Rtn1-mCherry::HIS3 pah1Δ::hph*	this study
SSY2808	*Sec63-mNeon::kan Rtn1-mCherry::HIS3 ice2Δ::nat pah1Δ::hph*	this study
SSY2229	*YMG1 Sec63-mNeon::URA3 Rtn1-mCherry::kan ice2Δ::nat*	this study
SSY2230	*YMG5 Sec63-mNeon::URA3 Rtn1-mCherry::kan ice2Δ::nat*	this study
SSY2256	*YMG5 Sec63-mNeon::URA3 Rtn1-mCherry::kan*	this study
SSY2482	*Sec63-mNeon::kan Rtn1-mCherry::HIS3 nem1Δ::hph*	this study
SSY2484	*Sec63-mNeon::kan Rtn1-mCherry::HIS3 ice2Δ::nat nem1Δ::hph*	this study
SSY2481	*Sec63-mNeon::kan Rtn1-mCherry::HIS3 spo7Δ::hph*	this study
SSY2483	*Sec63-mNeon::kan Rtn1-mCherry::HIS3 ice2Δ::nat spo7Δ::hph*	this study
SSY2480	*Sec63-mNeon::kan Rtn1-mCherry::HIS3 dgk1Δ::nat*	this study
SSY2485	*Sec63-mNeon::kan Rtn1-mCherry::HIS3 spo7Δ::hph Δdgk1::nat*	this study
SSY2486	*Sec63-mNeon::kan Rtn1-mCherry::HIS3 nem1Δ::hph Δdgk1::nat*	this study
SSY2822	*Sec63-mNeon::kan Rtn1-mCherry::HIS3 dgk1Δ::nat Δpah1::hph*	this study
SSY2592	*Pah1-3HA::HIS3*	this study
SSY2593	*Pah1-3HA::HIS3 ice2Δ::nat*	this study
SSY2594	*Pah1-3HA::HIS3 nem1Δ::nat*	this study
SSY2718	*Pah1-3HA::HIS3 ice2Δ::nat nem1Δ::hph*	this study
SSY2809	*pah1Δ::URA3*	this study
SSY2836	*Pah1-3HA*	this study
SSY2837	*pah1(7A)-3HA*	this study
SSY2841	*Pah1-3HA Sec63-mNeon::kan Rtn1-mCherry::HIS3*	this study
SSY2842	*pah1(7A)-3HA Sec63-mNeon::kan Rtn1-mCherry::HIS3*	this study
SSY2843	*Pah1-3HA Sec63-mNeon::kan Rtn1-mCherry::HIS3 ura3::P_{ADH1}-Ice2-LEU2*	this study
SSY2844	*pah1(7A)-3HA Sec63-mNeon::kan Rtn1-mCherry::HIS3 ura3::P_{ADH1}-Ice2-LEU2*	this study
SSY2588	*Sec63-mNeon::kan Rtn1-mCherry::HIS3 ura3::Padh-Ice2-LEU2*	this study

bioRxiv preprint doi: https://doi.org/10.1101/2020.02.23.961722; this version posted February 24, 2020. The copyright holder for this preprint (which was not certified by peer review) is the author/funder, who has granted bioRxiv a license to display the preprint in perpetuity. It is made available under aCC-BY-NC-ND 4.0 International license.

SSY2596	*Sec63-mNeon::kan Rtn1-mCherry::HIS3 ura3::Padh-Ice2-LEU2 opi1Δ::hph*	this study
SSY2805	*Sec63-mNeon::kan Rtn1-mCherry::HIS3 hac1Δ::hph*	this study
SSY2806	*Sec63-mNeon::kan Rtn1-mCherry::HIS3 ice2Δ::nat hac1Δ::hph*	this study

bioRxiv preprint doi: https://doi.org/10.1101/2020.02.23.961722; this version posted February 24, 2020. The copyright holder for this preprint (which was not certified by peer review) is the author/funder, who has granted bioRxiv a license to display the preprint in perpetuity. It is made available under aCC-BY-NC-ND 4.0 International license.

Figure 1

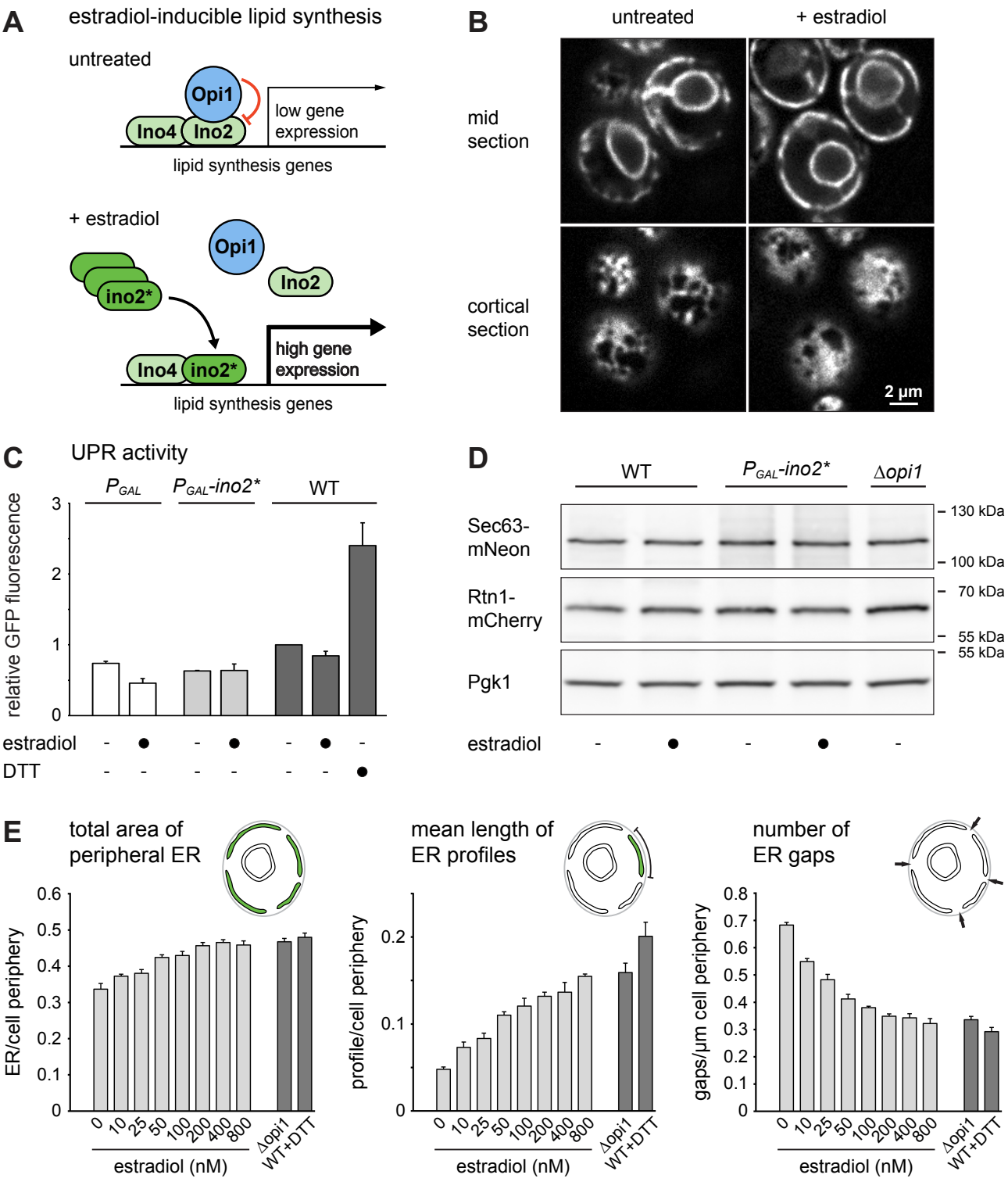

bioRxiv preprint doi: https://doi.org/10.1101/2020.02.23.961722; this version posted February 24, 2020. The copyright holder for this preprint (which was not certified by peer review) is the author/funder, who has granted bioRxiv a license to display the preprint in perpetuity. It is made available under aCC-BY-NC-ND 4.0 International license.

Figure 2

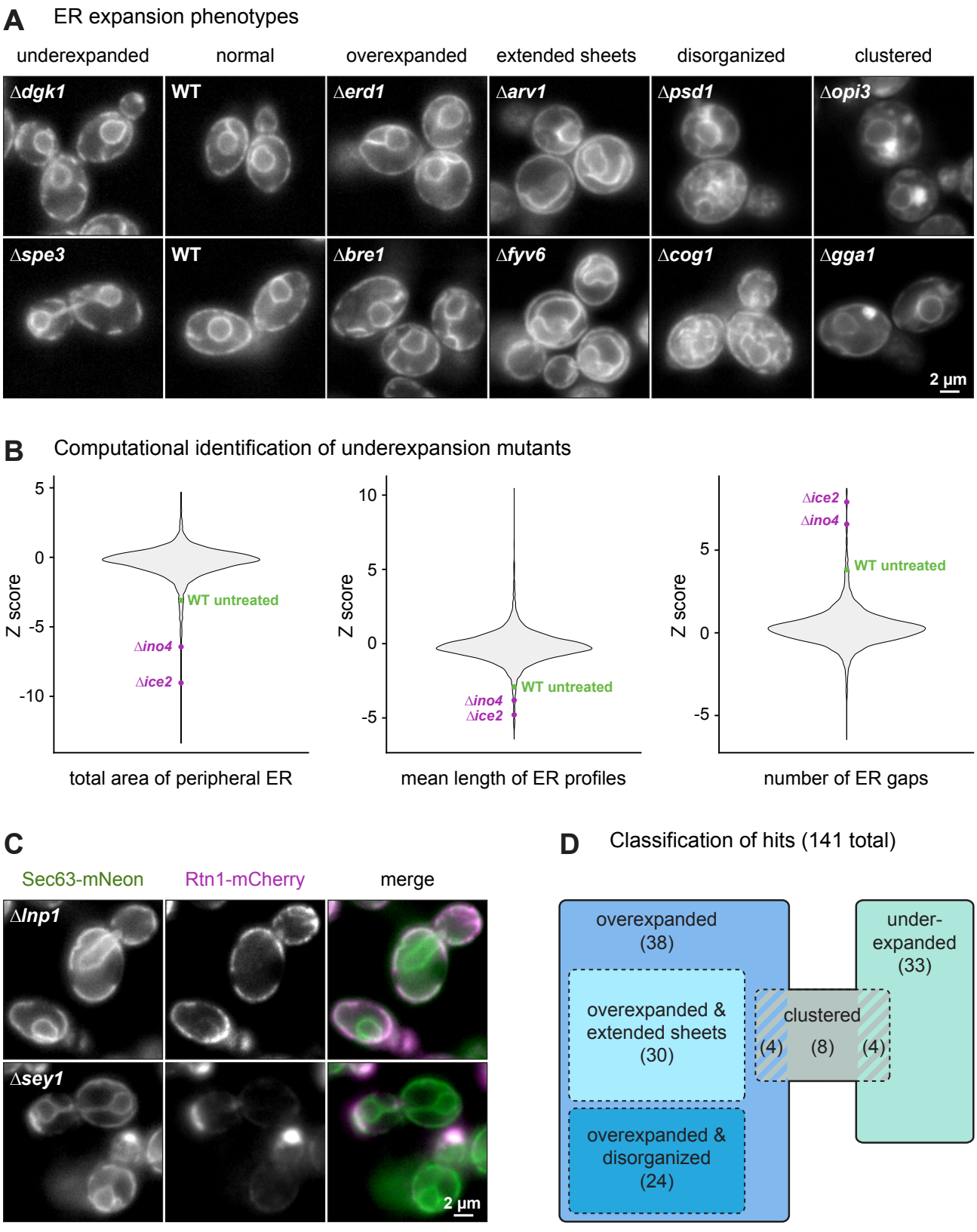

bioRxiv preprint doi: https://doi.org/10.1101/2020.02.23.961722; this version posted February 24, 2020. The copyright holder for this preprint (which was not certified by peer review) is the author/funder, who has granted bioRxiv a license to display the preprint in perpetuity. It is made available under aCC-BY-NC-ND 4.0 International license.

Figure 3

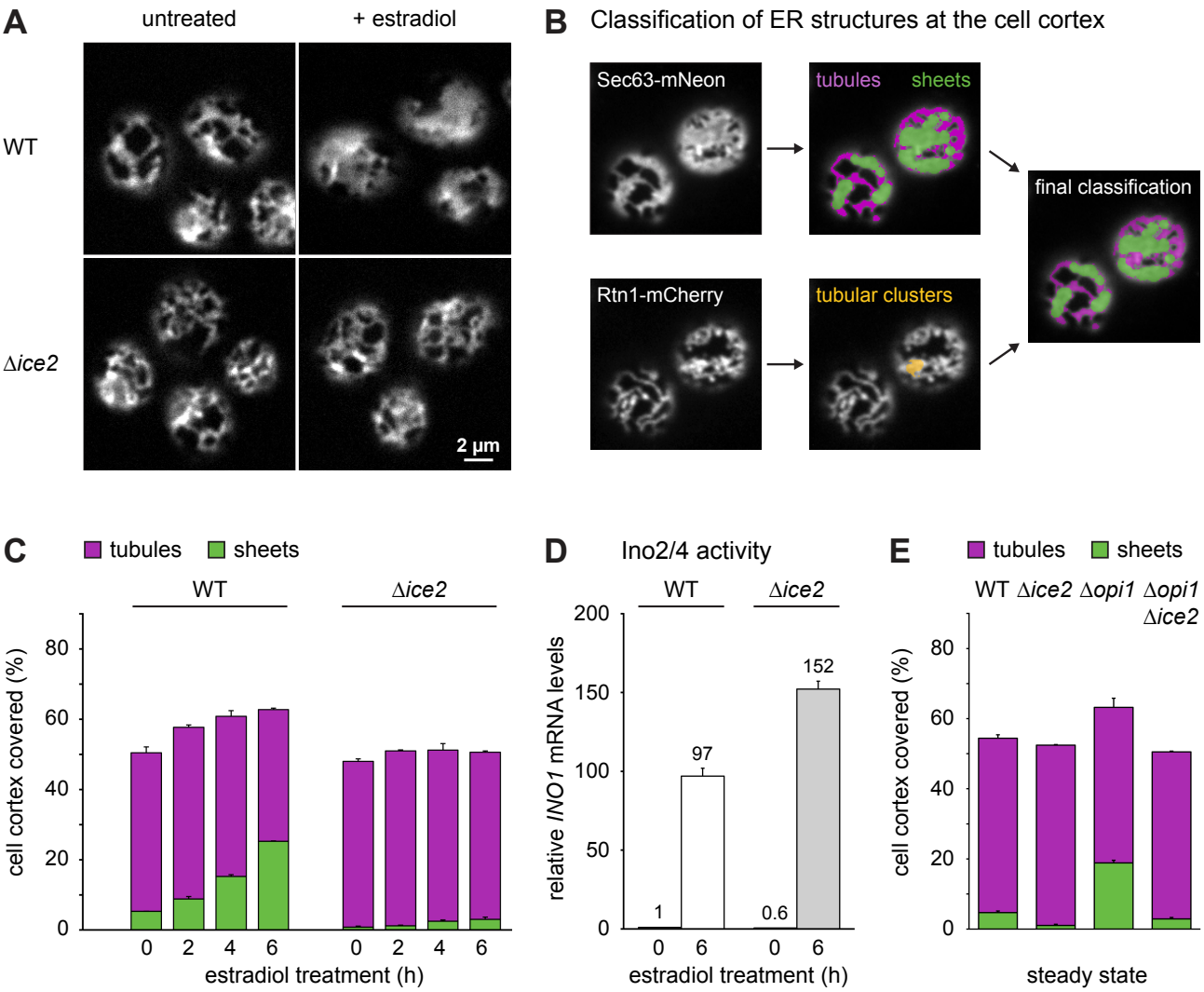

bioRxiv preprint doi: https://doi.org/10.1101/2020.02.23.961722; this version posted February 24, 2020. The copyright holder for this preprint (which was not certified by peer review) is the author/funder, who has granted bioRxiv a license to display the preprint in perpetuity. It is made available under aCC-BY-NC-ND 4.0 International license.

Figure 4

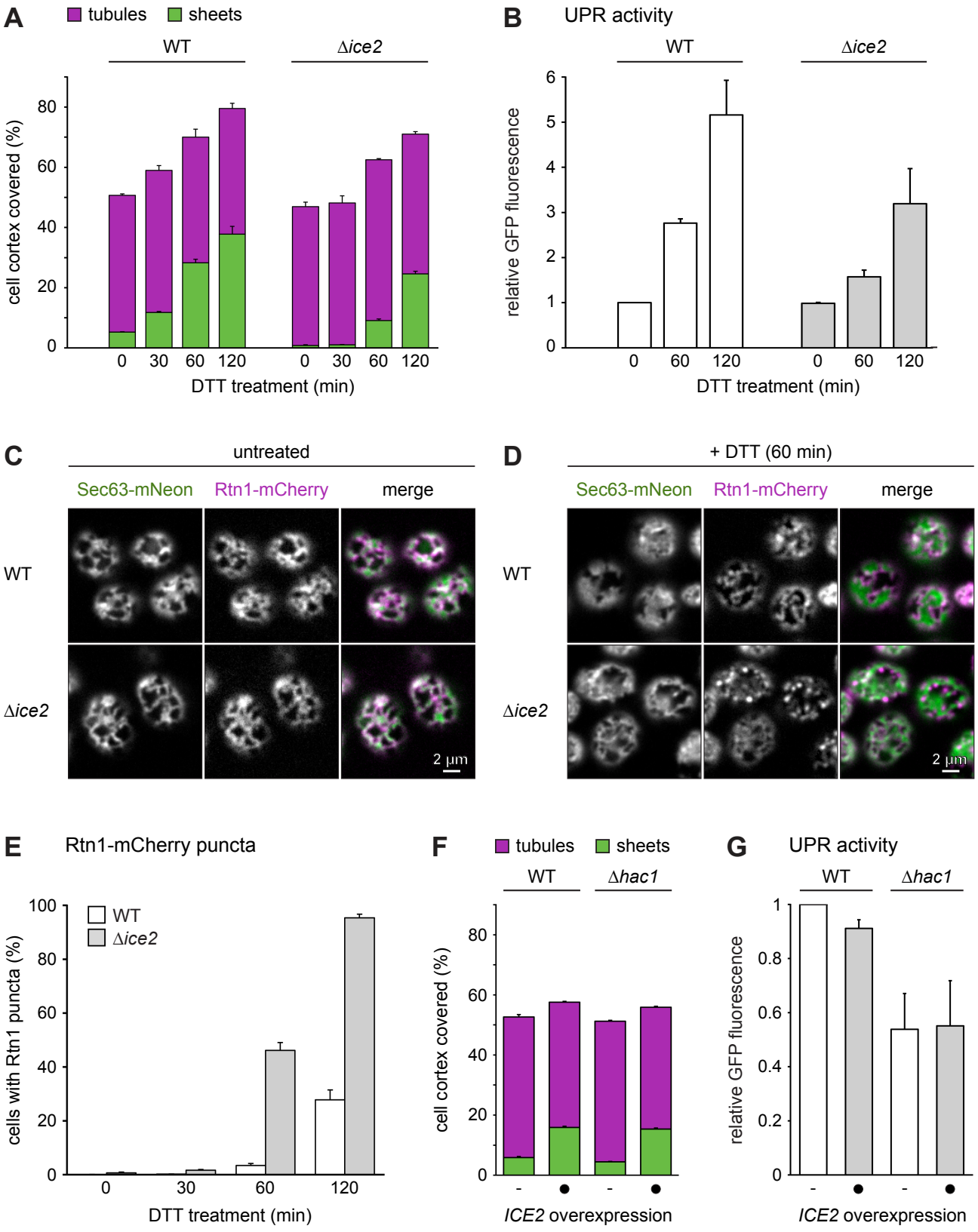

bioRxiv preprint doi: https://doi.org/10.1101/2020.02.23.961722; this version posted February 24, 2020. The copyright holder for this preprint (which was not certified by peer review) is the author/funder, who has granted bioRxiv a license to display the preprint in perpetuity. It is made available under aCC-BY-NC-ND 4.0 International license.

Figure 5

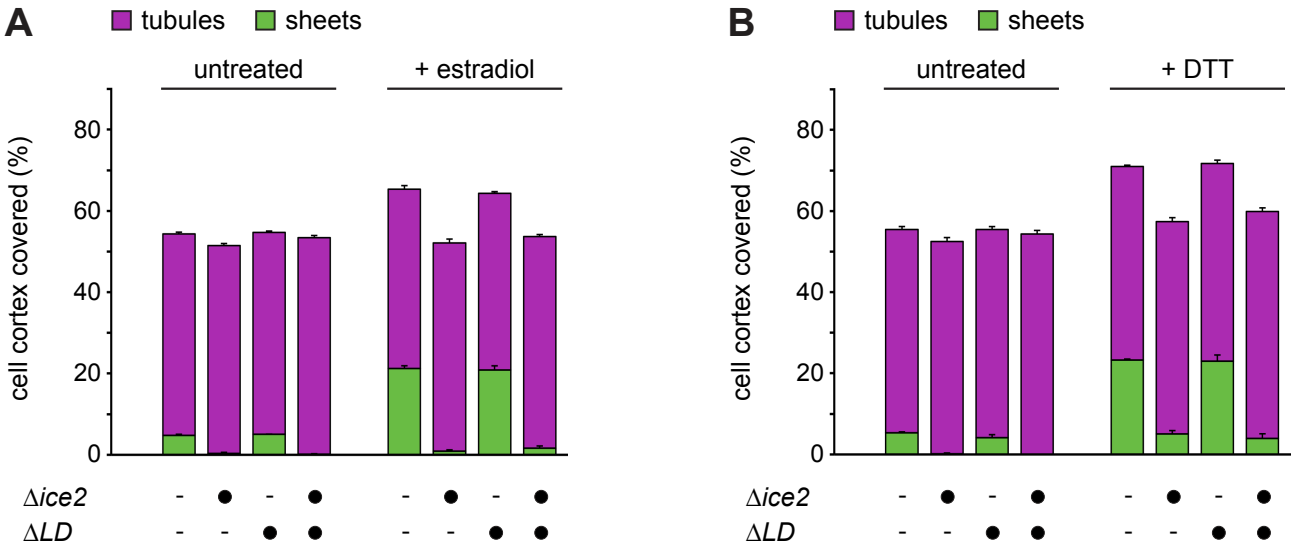

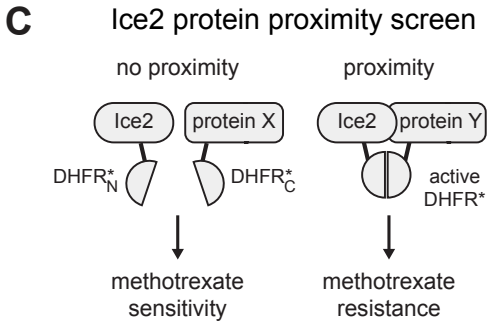

category	proteins
lipid metabolism	Cho1, Csg2, Elo1, Erg25, Ice2, Orm1, Phs1, Pis1, Sac1, Scs7, Spo7, Tsc13
protein targeting	Emc1, Emc3, Erp1, Got1, Shr3, Srp102, Yip3
protein glycosylation	Alg5, Ost1, Ost4, Wbp1
ER morphogenesis	Rtn1, Yop1
other/unknown function	Irc22, Ist2, Per33, Pmr1, Ubp1, Ypr114w
not an ER protein	Ccw12, Dfg5, Rpl22A, Rpl38, Zeo1, Ynl190w

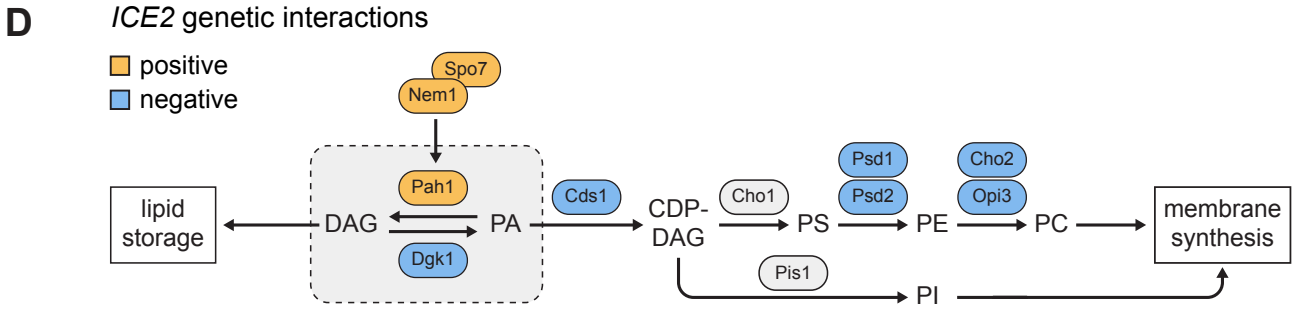

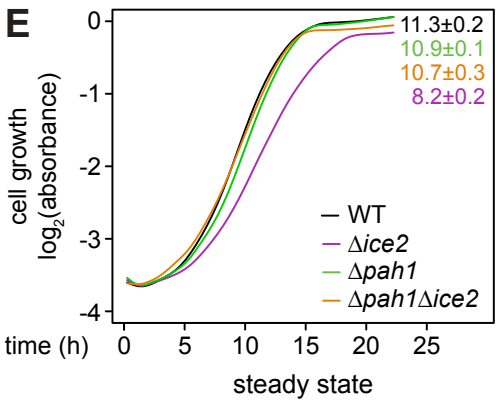

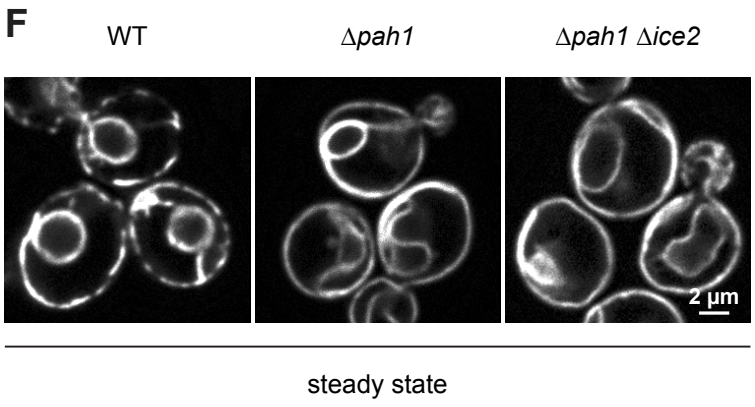

bioRxiv preprint doi: https://doi.org/10.1101/2020.02.23.961722; this version posted February 24, 2020. The copyright holder for this preprint (which was not certified by peer review) is the author/funder, who has granted bioRxiv a license to display the preprint in perpetuity. It is made available under aCC-BY-NC-ND 4.0 International license.

Figure 6

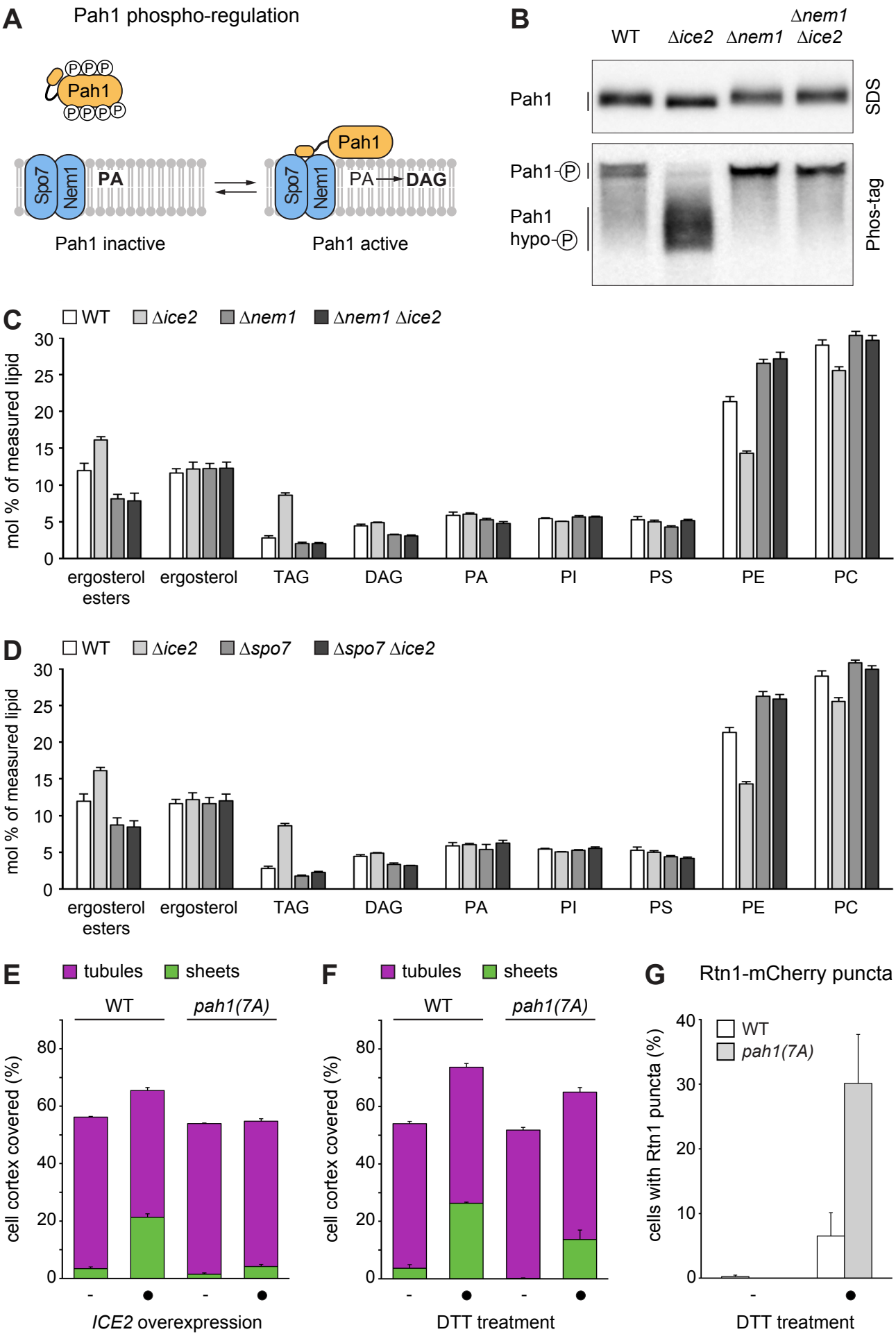

bioRxiv preprint doi: https://doi.org/10.1101/2020.02.23.961722; this version posted February 24, 2020. The copyright holder for this preprint (which was not certified by peer review) is the author/funder, who has granted bioRxiv a license to display the preprint in perpetuity. It is made available under aCC-BY-NC-ND 4.0 International license.

Figure 7

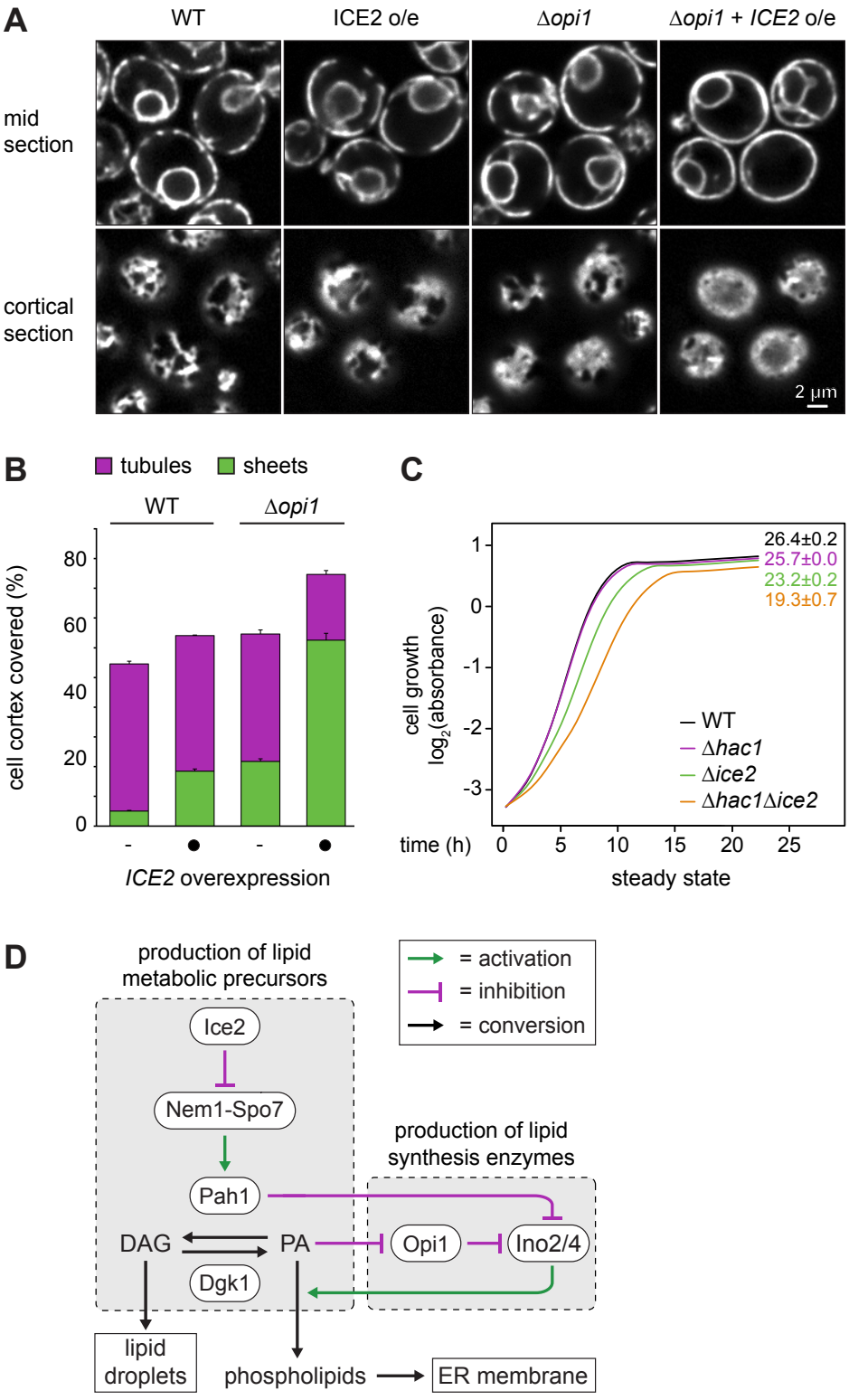

bioRxiv preprint doi: https://doi.org/10.1101/2020.02.23.961722; this version posted February 24, 2020. The copyright holder for this preprint (which was not certified by peer review) is the author/funder, who has granted bioRxiv a license to display the preprint in perpetuity. It is made available under aCC-BY-NC-ND 4.0 International license.

Figure S1

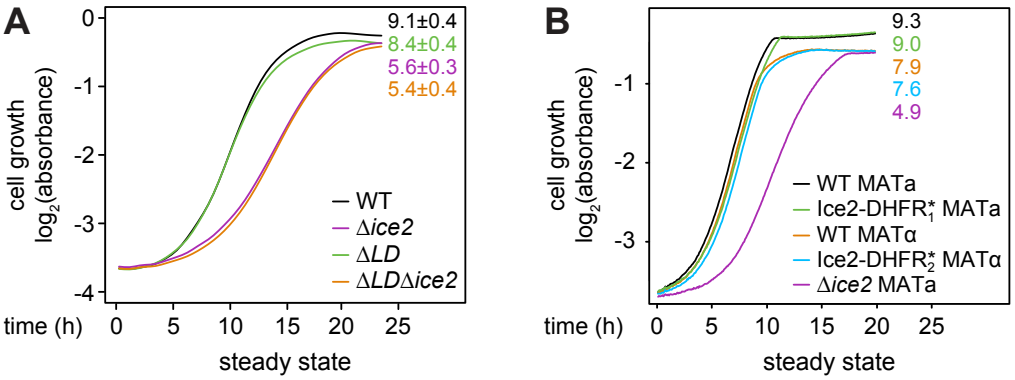

bioRxiv preprint doi: https://doi.org/10.1101/2020.02.23.961722; this version posted February 24, 2020. The copyright holder for this preprint (which was not certified by peer review) is the author/funder, who has granted bioRxiv a license to display the preprint in perpetuity. It is made available under aCC-BY-NC-ND 4.0 International license.
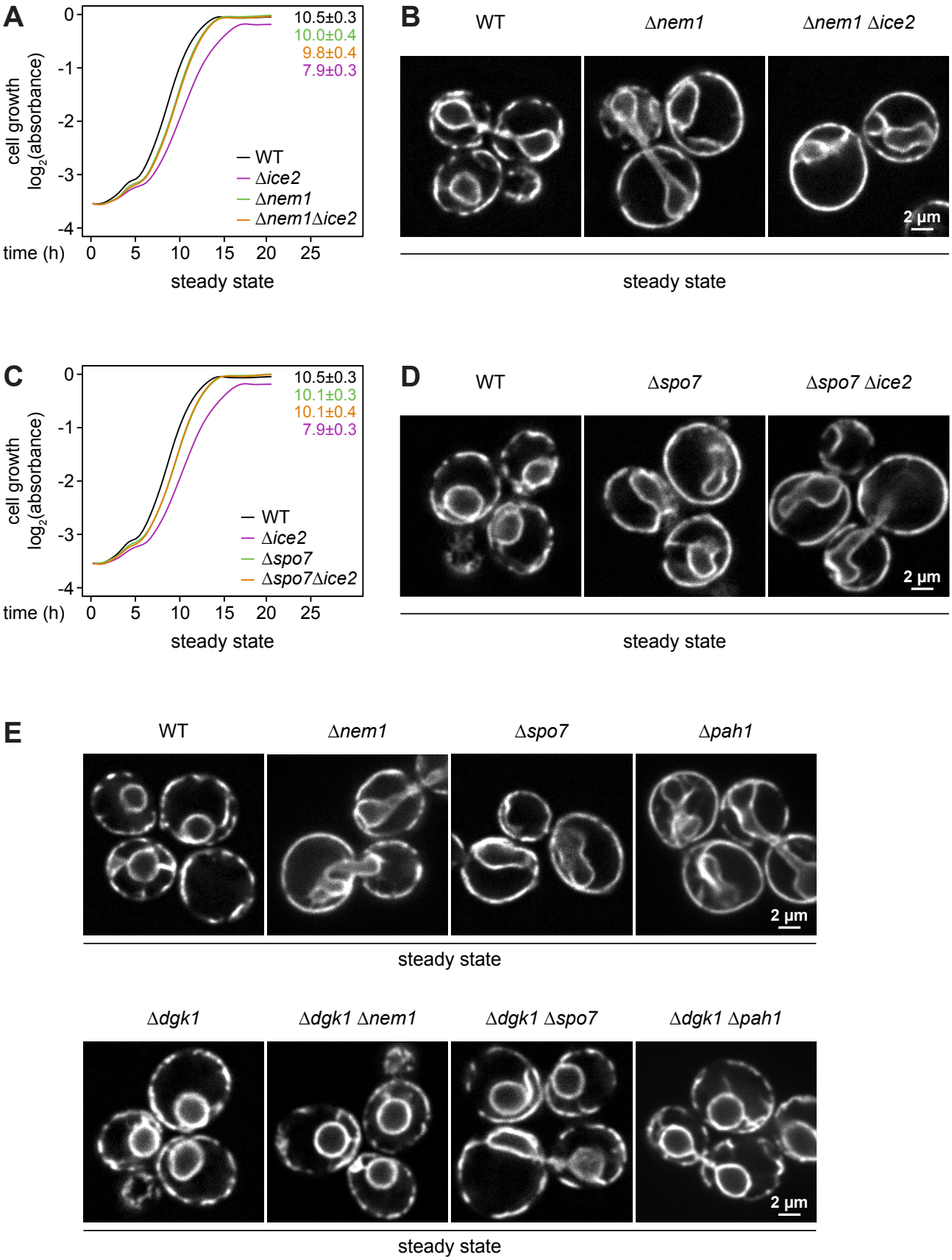
Figure S2